JOURNAL OF GEOPHYSICAL RESEARCH: SPACE PHYSICS, VOL. 118, 82–98, doi:10.1029/2012JA017923, 2013

Transport of the plasma sheet electrons to the geostationary distances

N. Y. Ganushkina,[1,2] O. A. Amariutei,[1] Y. Y. Shprits,[3,4] and M. W. Liemohn[2]

Received 7 May 2012; revised 15 September 2012; accepted 27 October 2012; published 31 January 2013.

[1] The transport and acceleration of low-energy electrons (50–250 keV) from the plasma sheet to the geostationary orbit were investigated. Two moderate storm events, which occurred on 6–7 November 1997 and 12–14 June 2005, were modeled using the Inner Magnetosphere Particle Transport and Acceleration model (IMPTAM) with the boundary set at 10 R_E in the plasma sheet. The output of the IMPTAM was compared to the observed electron fluxes in four energy ranges (50–225 keV) measured by the Synchronous Orbit Particle Analyzer instrument onboard the Los Alamos National Laboratory spacecraft. It was found that the large-scale convection in combination with substorm-associated impulsive fields is the drivers of the transport of plasma sheet electrons from 10 R_E to geostationary orbit at 6.6 R_E during storm times. The addition of radial diffusion had no significant influence on the modeled electron fluxes. At the same time, the modeled electron fluxes are one (two) order (s) smaller than the observed ones for 50–150 keV (150–225 keV) electrons, respectively, most likely due to inaccuracy of electron boundary conditions. The loss processes due to wave-particle interactions were not considered. The choice of the large-scale convection electric field model used in simulations did not have a significant influence on the modeled electron fluxes, since there is not much difference between the equipotential contours given by the Volland-Stern and the Boyle *et al*. (1997) models at distances from 10 to 6.6 R_E in the plasma sheet. Using the TS05 model for the background magnetic field instead of the T96 model resulted in larger deviations of the modeled electron fluxes from the observed ones due to specific features of the TS05 model. The increase in the modeled electron fluxes can be as large as two orders of magnitude when substorm-associated electromagnetic fields were taken into account. The obtained model distribution of low-energy electron fluxes can be used as an input to the radiation belt models. This seed population for radiation belts will affect the local acceleration up to relativistic energies.

Citation: Ganushkina, N. Y., O. A. Amariutei, Y. Y. Shprits, and M. W. Liemohn (2013), Transport of the plasma sheet electrons to the geostationary distances, *J. Geophys. Res. Space Physics*, *118*, 82–98, doi:10.1029/2012JA017923.

1. Introduction

[2] The distribution of low-energy electrons with energies from approximately 10 to 250 keV, which is the seed population, is critically important for the radiation belt dynamics. During periods with sufficiently high phase space density in the plasma sheet [e.g., *Huang and Frank*, 1986; *Christon et al*., 1989; *Taylor et al*., 2004] and strong convective driving, these particles may serve as a source of MeV particles. Radiation belt models need to specify the flux at a low-energy boundary at all *L*-shells. Quite often, the lower energy boundary condition is fixed at several keV. However, the electron flux at these energies varies significantly with geomagnetic activity. Satellite measurements cannot provide continuous measurements of tens to a few hundreds of keV at all magnetic local time (MLT) and *L*-shells.

[3] An examination of near-Earth and plasma sheet densities, temperatures, and entropies showed that the plasma sheet is usually spatially homogeneous [*Borovsky et al*., 1998]. *Friedel et al*. [2001] analyzed the electron data from the Polar HYDRA instrument [*Scudder et al*., 1995] with the coverage of the inner magnetospheric region at radial distances from 2 to 9 R_E and geosynchronous data measured by the Los Alamos National Laboratory (LANL) Magnetospheric Plasma Analyzer (MPA) [*Bame et al*., 1993]. They showed that the simple corotation and convection electric field can describe rather well the average properties of transport for these particles for a wide range of geomagnetic activity and over a large part of the inner magnetosphere. Recently, *Kurita et al*. [2011], using the electron data from the THEMIS spacecraft from 2007 to 2009, derived global phase space density (PSD) distributions of plasma sheet electrons (2–100 eV/nT) to examine the transport process of the electrons into the inner magnetosphere and possible

[1]Finnish Meteorological Institute, Helsinki, Finland.
[2]Department of Atmospheric, Oceanic and Space Sciences, University of Michigan, Ann Arbor, Michigan, USA.
[3]Department of Earth and Space Sciences and Institute of Geophysics and Planetary Physics, University of California, Los Angeles, Los Angeles, California, USA.
[4]Institute of Geophysics and Planetary Physics and Department of Atmospheric and Oceanic Sciences, Los Angeles, California, USA.

Corresponding author: N. Yu. Ganushkina, Finnish Meteorological Institute, Helsinki, Finland. (Natalia.Ganushkina@fmi.fi)

2169-9380/13/2012JA017923

loss mechanisms of plasma sheet electrons during convective transport. They reconfirmed the previous results according to which the large-scale convection electric field controls the electron transport to the inner magnetosphere. The gradual decrease in PSD observed in the morning sector was attributed to the existence of the loss of plasma sheet electrons as a result of pitch angle scattering by whistler mode chorus. Particle tracing studies [e.g., *Elkington et al*., 2004] have shown that, during times of strong convection, tens of keV plasma sheet electrons can have access to geosynchronous orbit, and in the process of diffusion can be accelerated to MeV energies. Similarly, local acceleration depends on injection of plasma sheet electrons into near-Earth space [e.g., *Mauk and Meng*, 1983; *Kerns et al*., 1994; *Shprits et al*., 2009]. *Miyoshi et al*. [2006] combined the relativistic ring current-atmosphere interactions model (RAM) [*Jordanova et al*., 1996, 2003], which reproduces the convective transport of electrons with a radial diffusion model to simulate the October 2001 storm. Their study concluded that additional in situ energization was required to explain the observations.

[4] Several studies have shown that during disturbed conditions earthward transport of plasma and magnetic flux occurs in the form of short-duration, high-speed plasma flows, rather than as slow, steady convection [*Baumjohann et al*., 1990; *Angelopoulos et al*., 1992]. Recently, there have been quite a few studies on the dipolarization fronts observed during substorms [*Sergeev et al*., 2009; *Runov et al*., 2011, 2012; *Birn et al*., 2012]. The main observational characteristics of these fronts include [*Runov et al*., 2012]:

[5] (1) rapid ($\sim$1 to a few seconds) increase in B_z accompanied by rapid decrease in the plasma density, often preceded by a short B_z dip and followed by gradual B_z decrease at time scale of a minute;

[6] (2) enhancement in electric field (up to $\sim$10 mV/m) during a few tens of seconds;

[7] (3) gradual increase in energetic ion flux, which stars $\sim$30 s ahead of the front;

[8] (4) rapid, step-like increase or decrease in energetic electron flux.

There is no definite answer about the relationship (if any) between the fronts and the global substorm dipolarization observed at geosynchronous orbit. There exist some assumptions that the substorm dipolarization is a cumulative effect of braking fronts [*Lyons et al*., 2012]. However, there is not enough evidence for that.

[9] At the same time, there exist observational and modeling results for the electric fields in different scales in the inner magnetosphere during substorms and storms. Substorms often occur during storms, and together with the large-scale convection electric field, smaller-scale inductive electric fields make their contribution to particle transport and acceleration in the plasma sheet. Observations show that substorm-associated electric fields usually display a very complicated behavior [*Maynard et al*., 1996]. The intense electric fields with a strong impulsive component with amplitudes of up to even several tens of mV/m have been detected deep in the inner magnetosphere (3–4 R_E) during the substorm onset [*Shepherd et al*., 1980; *Aggson et al*., 1983; *Cattell and Mozer*, 1984; *Wygant et al*., 1998; *Rowland and Wygant*, 1998; *Tu et al*., 2000]. These fields were found to be coincident with braking of the fast flows and correlated with magnetic field dipolarization in the inner central plasma sheet [*Slavin et al*., 2002; *Nakamura et al*., 2002]. At the same time, dipolarization fronts do not penetrate deeper than geostationary distances (A. Runov, private communication, 2012). The origin of strong transient electric fields at substorm onset and their detailed relationship to the magnetic field dipolarization is still an open question.

[10] Substorms are generally associated with injection of electrons of energy up to only a few hundred keV [*Cayton et al*., 1989; *Baker et al*., 1989]. *Birn et al*. [1997, 1998] have investigated particle injections using geosynchronous observations and test particle tracing in the fields generated by a three-dimensional MHD simulation of the magnetotail neutral line formation and dipolarization. Test particle simulations by *Birn et al*. [1997, 1998] can explain the initial rise of the particle injection at geosynchronous orbit at different local times near midnight. Several models have been proposed to explain particle injections [*Li et al*., 1998; *Zaharia et al*., 2000; *Sarris et al*., 2002]. The models are built on the idea that a perturbation farther out in the magnetotail propagates inward, probably in the form of bursty bulk flows, and produces dipolarization and dispersionless injections. So far these models give good agreement with the observed dispersionless electron injections at geostationary orbit [*Ingraham et al*., 2001; *Li et al*., 2003; *Mithaiwala and Horton*, 2005; *Liu et al*., 2009]. *Glocer et al*. [2011] made simulations with the Space Weather Modeling Framework [*Tóth et al*., 2005] configured with global magnetosphere, radiation belt, ring current, and ionosphere electrodynamics model. They concluded that storm-time dipolarization events in the magnetospheric magnetic field result in strong radial transport and energization of radiation belt electrons.

[11] Although many studies address the modeling of the electron injections from the plasma sheet, the question of the relative importance of the large-scale convection and substorm-associated fields in the transport and acceleration of low energy electrons of less than 100 keV from the near-Earth plasma sheet to the geostationary orbit remains open. Another important factor for relativistic electron dynamics is the background conditions in the inner magnetosphere. Magnetic field distortions lead to huge reductions in particle flux (known as the *Dst* effect [*Kim and Chan*, 1997]), and the topology of this field depends on the ring current [*Parker and Stewart*, 1967; *Tsyganenko and Sitnov*, 2005] and near-Earth tail current [*Ganushkina et al*., 2010].

[12] In the present paper, we investigate the low energy electron (50–250 keV) transport and acceleration from the plasma sheet to geostationary orbit. We specifically study the roles of large-scale convection and substorm-associated fields. We use the Inner Magnetosphere Particle Transport and Acceleration model (IMPTAM) [*Ganushkina et al*., 2005, 2006, 2012b] with the boundary at 10 R_E in the plasma sheet, where we set boundary conditions for the low-energy electrons following *Tsyganenko and Mukai* [2003]. We model two moderate storm events, which occurred on 6–7 November 1997 and 12-14 June 2005. We follow the evolution of the electron distribution function from 10 R_E to 6.6 R_E in two different magnetic field models and two electric field models. Moreover, we launch a series of

substorm-associated electromagnetic pulses at substorm onsets to represent the changes, which occur during substorm dipolarizations. The output of the IMPTAM modeling is compared to the observed electron fluxes in four energy ranges (50–250 keV) measured onboard the LANL spacecraft by the Synchronous Orbit Particle Analyzer (SOPA) instrument [*Belian et al.*, 1992]. The obtained model distribution of low-energy electron fluxes can be used as an input to the radiation belts models for local acceleration up to relativistic energies and for modulating the relativistic electron phase space density.

2. Storm Event Overview

[13] Two moderate storm events were selected for the present study. Figure 1 presents an overview of the first modeled coronal mass ejection (CME)-driven storm, which occurred on 6–7 November 1997. The solar wind and the interplanetary magnetic field (IMF) data were obtained from the Wind spacecraft, including about 40 min time shift for propagation to the Earth's magnetopause. The *AE*, *Kp*, and *SymH* indices data were obtained from the World Data Center C2 for Geomagnetism, Kyoto. As seen in Figure 1, the storm that occurred on 6–7 November 1997 was of a moderate intensity. On 6 November, the IMF B_z (Figure 1a) fluctuated around 0 and dropped to −15 nT at the end of the day at around 2300 UT. Together with the B_z drop, at 2210 UT there was an increase of the V_x component of the solar wind speed (Figure 1b) from 330 km/s up to 460 km/s. On the same day, 6 November, the solar wind dynamic pressure (Figure 1c) was about 3 nPa, increasing up to about 10 nPa at about 2200 UT. The *AE* index (Figure 1d) had several peaks with its highest magnitudes of about 1300 nT at 0200 UT and 1500 nT at 0500 UT on 7 November. The *Kp* index (Figure 1e) reached 7 during the storm maximum. The *SymH* index (Figure 1f) reached −120 nT at about 0400 UT on 7 November and recovered to −20 nT by the end of the day.

[14] Figure 2 presents an overview of the second modeled storm, which occurred on 12–14 June 2005. This storm was also a CME storm, when IMF B_z (Figure 2a) fluctuated around zero in the beginning of 12 June, then turned negative around 1330 UT and reached −15 nT for a short time, then went northward and finally dropped from +10 nT to −15 nT at 1700 UT and stayed negative till the end of 13 June. At the same time with the variations and drop of IMF B_z, the V_x component (Figure 2b) of the solar wind speed increased from 320 km/s up to 490 km/s. Solar wind dynamic pressure (Figure 2c) showed a peak of 12 nPa around 0820 and 0950 UT and later of 10 nPa at 1640 UT on 12 June. The *AE* index (Figure 2d) had several peaks with its highest magnitudes of 2000 nT at 1850 UT on 12 June and later with a magnitude of about 1400 nT on 13 June. The *Kp* index (Figure 2e) reached 7 during the storm main phase. The *SymH* index (Figure 2f) started to drop from positive to negative values at 1745 UT on 12 June and reached −110 nT at about 0330 UT on 13 June and recovered to −10 nT by the end of 14 June.

3. Modeling Approach

3.1. Inner Magnetosphere Particle Transport and Acceleration Model

[15] The Inner Magnetosphere Particle Transport and Acceleration Model (IMPTAM), developed by *Ganushkina et al*. [2001]; *Ganushkina et al*. [2005, 2006], follows distributions of ions and electrons with arbitrary pitch angles from the plasma sheet to the inner *L*-shell regions with energies

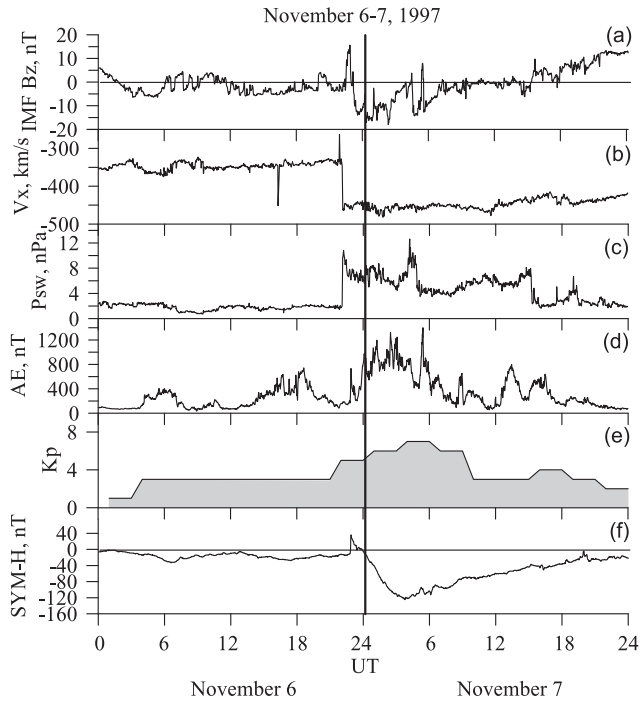

Figure 1. Overview of modeled magnetic storm on 6–7 November 1997 (see text).

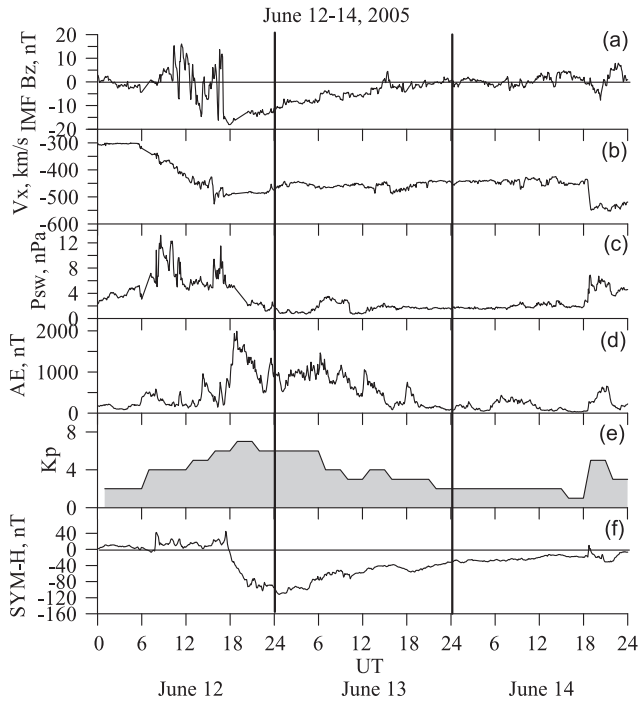

Figure 2. Overview of modeled magnetic storm on 12–14 June 2005 (see text).

reaching up to hundreds of keVs in time-dependent magnetic and electric fields. The detailed description was presented recently in *Ganushkina et al*. [2012b]. We trace a distribution of particles in the guiding center, or drift, approximation, and the drift velocities are considered such that relativistic effects for electrons are taken into account.

[16] The drift velocity is a combination of the velocity $V_{E\times B}$ due to $\mathbf{E}\times\mathbf{B}$ drift $V_{E\times B}=(\mathbf{E}\times\mathbf{B})/\mathbf{B}^2$, where $\mathbf{E}$ and $\mathbf{B}$ are electric and magnetic fields, respectively, and the velocities of gradient V_∇ and curvature V_{cur} drifts $V_\nabla + V_{\mathrm{cur}} = \left(mv_\perp^2\right)/(2qB^2)\ (\mathbf{B}\times\nabla\mathbf{B}) + \left(mv_\parallel^2\right)/\left(qR_c^2B^2\right)\ (\mathbf{R_c}\times\mathbf{B})$ [*Roederer*, 1970], where m is the particle mass, q is the particle charge, $v_\perp$ and $v_\parallel$ are the particle velocities perpendicular and parallel to the magnetic field, respectively, R_c is the radius of curvature of the magnetic field line ($\nabla_\perp B = -(B/R_c)\mathbf{n}$, where $\mathbf{n}$ is the unit normal vector along the radius of curvature). We assume that the first and second adiabatic invariants are conserved. We consider the bounce-average drift velocity after averaging over one bounce of $\mathbf{E}\times\mathbf{B}$ magnetic drift velocities [*Roederer*, 1970]

$$\langle v_0\rangle = \frac{\mathbf{E}_0\times\mathbf{B}_0}{B_0^2} + \frac{2p}{q\tau_b B_0}\nabla I\times\mathbf{e}_0, \tag{1}$$

where $\mathbf{E}_0$ and $\mathbf{B}_0$ are the electric and magnetic fields in the equatorial plane, respectively, p is the particle's momentum, τ_b is the particle's bounce period, $I=\int_{S_m}^{S'_m}\left[1-\frac{B(s)}{B_m}\right]^{1/2}ds$, S_m and S'_m are the mirror points, $B(s)$ is the magnetic field along magnetic field line, B_m is the magnetic field at the mirror point, and $\mathbf{e}_0$ is the unit vector in the direction of the magnetic field $\mathbf{B}_0$.

[17] The changes in the distribution function $f(R,\phi,t,E_{\mathrm{kin}},\alpha)$, where R and ϕ are the radial and azimuthal coordinates in the equatorial plane, respectively, t is the time, E_{kin} is the particle energy, and α is the particle pitch angle, are obtained by solving the following equation:

$$\frac{df}{dt} = \frac{\partial f}{\partial\phi}\cdot V_\phi + \frac{\partial f}{\partial R}\cdot V_R + \mathrm{sources} - \mathrm{losses}, \tag{2}$$

where V_ϕ and V_R are the azimuthal and radial components of the bounce-average drift velocity. Liouville's theorem is used to gain information of the entire distribution function with losses taken into account.

[18] If we know the distribution function $f(R,\phi,t,E_{\mathrm{kin}},\alpha)$ of particles at a time moment t_1, then we can obtain the distribution function of particles at a time moment $t_2=t_1+\Delta t$, by computing the drift velocity of the particles. The distribution function at t_2 will not be the same as at t_1 at the corresponding positions, since we need to take into account the phase-space-dependent losses (τ_{loss}). The final distribution function at t_2 will be $f(t_2)=f(t_1)\exp(-\Delta t/\tau_{\mathrm{loss}})$.

[19] After that for the obtained distribution, we apply another process that IMPTAM is able to take into account, which is the radial diffusion. Radial diffusion plays a role in electron energization [*Fälthammar*, 1965; *Schulz and Lanzerotti*, 1974; *Brautigam and Albert*, 2000]. We solve the radial diffusion equation [*Schulz and Lanzerotti*, 1974] for the distribution function from equation (2):

$$\frac{\partial f}{\partial t} = L^2\frac{\partial}{\partial L}\left(L^{-2}D_{LL}\frac{\partial f}{\partial L}\right) - \frac{f}{\tau_{eL}}, \tag{3}$$

where τ_{eL} is the electron lifetime, and D_{LL} is the radial diffusion coefficient. Kp-dependent radial diffusion coefficients D_{LL} for the magnetic field fluctuations are computed following *Brautigam and Albert* [2000] using

$$D_{LL} = 10^{0.056Kp-9.325}L^{10}. \tag{4}$$

Since diffusion by the magnetic field fluctuations at $L>3$ dominates diffusion produced by electrostatic field fluctuations [*Shprits and Thorne*, 2004], we ignore the electrostatic component of the radial diffusion coefficient.

[20] At the next time step we repeat the order of calculation: first we solve transport with losses with equation (2) and then apply the diffusion with equation (3).

[21] The purpose of this study is to investigate how the convection and substorm-associated fields can bring plasma sheet electrons inward; thus, we neglect losses and assume that electron lifetime τ_{eL} is infinite and consider only convection outflow as a loss process when following the low-energy electrons from $10\,R_E$ to $6.6\,R_E$.

3.2. Representations for Boundary Conditions and Magnetic and Electric Fields Used in Simulations

[22] To study the transport of the plasma sheet electrons to geostationary orbit, we set the model boundary at $10\,R_E$. For the electron distribution at the boundary we used a kappa distribution function with n and T given by the empirical model derived from Geotail data by *Tsyganenko and Mukai* [2003]. The electron number density is assumed to be the same as that for ions in the model. However, for the electron temperature, the correction factor $Te/Ti=0.2$ is taken into account (as was shown, for example, in *Kaufmann et al*. [2005] and *Wang et al*. [2012], based on Geotail and THEMIS data). We also introduced a time shift of 2 h following *Borovsky et al*. [1998], who found that solar wind material reaches the midtail plasma sheet in about 2 h by investigating the time lags between the solar wind density and the plasma sheet density statistically and on a case-by-case basis.

[23] We set the model boundary at $10\,R_E$ at all MLTs with n and T given by *Tsyganenko and Mukai* [2003] model derived mainly for the nightside plasma sheet. This is not a problem, since on the dayside, the particles move outward, not inward, when we start to follow their motion. We trace the magnetic field lines and consider only closed magnetic field lines. If the particles happen to be on the open magnetic field lines, they are considered lost. So, the motion of the magnetopause (given, actually, by Tsyganenko magnetic field model used in calculations of the magnetic field lines) is taken into account and, therefore, the outflow loss too. Whatever the electric field is on the dayside, we follow the particles in it and in the magnetic field and follow only the particles which stay on the closed magnetic field lines.

[24] As an example, Figure 3 presents the perpendicular electron temperature in keV (Figure 3a) and number density at midnight (Figure 3c) as observed by LANL MPA instrument at geostationary orbit, the electron temperature in keV (Figure 3b) and number density at midnight (Figure 3d) as computed using the empirical model derived from Geotail

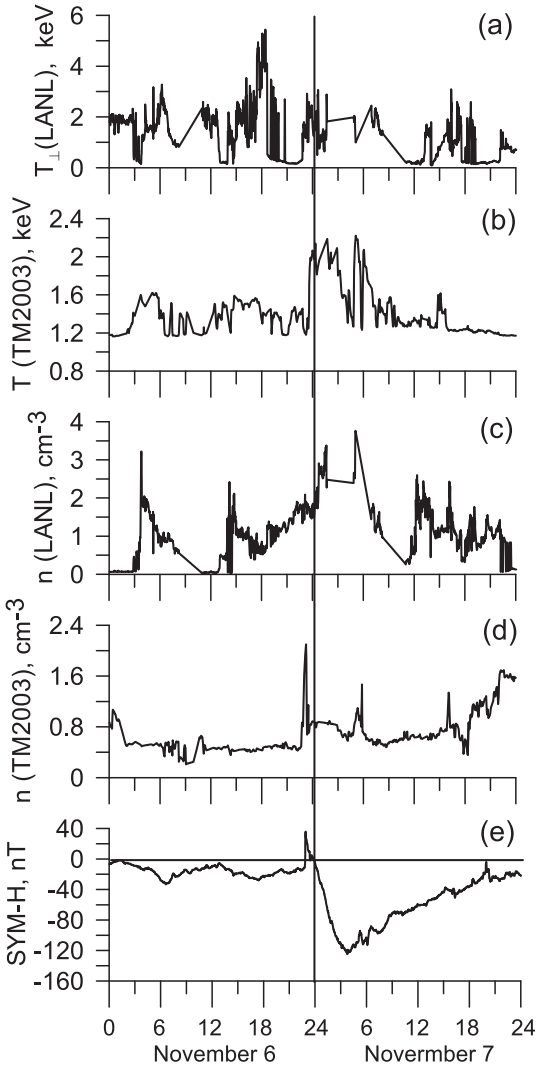

Figure 3. (a) Perpendicular electron temperature in keV as observed by LANL MPA instrument at geostationary orbit and (b) electron temperature in keV as computed using the empirical model derived from Geotail data by *Tsyganenko and Mukai* [2003], (c) number density from LANL MPA and (d) number density given by *Tsyganenko and Mukai* [2003] at midnight with (e) the observed *SymH* index for magnetic storm on 6–7 November 1997.

data by *Tsyganenko and Mukai* [2003], and the observed *SymH* index for magnetic storm on 6–7 November 1997 (Figure 3e). The number density n and perpendicular temperature ($T_\perp$) estimates at geostationary orbit (Figures 3a and 3c) were obtained using data from the LANL MPA instrument measuring ions in the energy range 0.1–40 keV. During the period of 6–7 November 1997 storm, data from four LANL spacecraft, 1990-095, 1991-080, 1994-084, and LANL-97A, were available. The number density and perpendicular and parallel temperatures were created from measurements obtained within 4 h of local time around midnight. Values were averaged when more than one spacecraft were simultaneously in that region. When no satellites were near midnight, the data were interpolated linearly.

[25] As expected, the model electron temperature and number density at $10\,R_E$ (Figures 3b and 3d) differ from those ones at $6.6\,R_E$, showing rather different time-dependent profiles and up to twice as high values at geostationary. It is very important to have an adequate model for time-dependent boundary conditions, when we study the electron transport from the plasma sheet. The *Tsyganenko and Mukai* [2003] model is the best we can use for time-dependent boundary conditions at $10\,R_E$ in the present study.

[26] The evolution of the modeled electron distributions was followed using combinations of several representations for magnetic and electric fields. We use a dipole model for the internal magnetic field. For the external magnetic field two different representations were used:

[27] (1) T96 [*Tsyganenko*, 1995] with *Dst*, P_{sw}, and IMF B_y and B_z as input parameters;

[28] (2) Tsyganenko and Sitnov TS05 [*Tsyganenko and Sitnov*, 2005] with *Dst*, P_{sw}, IMF B_y and B_z, and six variables $W_i, i=1,6$ as input parameters. The variables W enter in the six magnitude coefficients for the magnetic fields from each source and are calculated as time integrals dependent on solar wind and IMF parameters from the moment in time when IMF B_z turns southward.

[29] The electric field representations include

[30] (1) *Kp*-dependent Volland-Stern VS [*Volland*, 1973; *Stern*, 1975] convection electric field;

[31] (2) *Boyle et al*. [1997] polar cap potential dependent on solar wind and IMF parameters applied to a Volland-Stern type convection electric field pattern.

3.3. Substorm-Associated Impulsive Electric and Magnetic Fields

[32] One of the advantages of the IMPTAM model is the ability to simulate the full pitch-angle distribution of particles and utilize any magnetic or electric field configuration. In addition to the large-scale fields, transient fields associated with the dipolarization process in the magnetotail during substorm onset are included. The origin of strong transient electric fields at substorm onset and their detailed relationship to the magnetic field dipolarization is still an open question. However, several models have been proposed to explain particle injections [*Li et al*., 1998; *Zaharia et al*., 2000; *Sarris et al*., 2002]. In our study, we use *Li et al*. [1998] model with modifications for pulse velocity introduced by *Sarris et al*. [2002] to represent the dipolarization process. The dipolarization was modeled as an earthward-propagating electromagnetic pulse of localized radial and longitudinal extent. During this dipolarization process, the northward equatorial magnetic field increases due to a temporally and spatially varying westward electric field. The electric field is modeled as a time-dependent Gaussian pulse with a purely azimuthal electric field component that propagates radially inward at a decreasing velocity, decreases away from midnight, and is partially reflected near the plasmapause. The earthward propagation speed decreased as the pulse moved inward to mimic the breaking of the flows. According to *Li et al*. [1998], the pulse is present during about 10 min.

[33] In the spherical coordinate system (r,θ,ϕ), where $r=0$ at the center of the Earth, $\theta=0$ defines the equatorial

plane and $\phi = 0$ is at local noon (positive eastward), the electric field is given by

$$\mathbf{E}_{\varphi} = -\hat{e}_{\phi} E_0 (1 + c_1 \cos(\phi - \phi_0))^p \exp(-\xi^2) \quad (5)$$

where $\xi = [r - r_i + v(r)(t - t_a)]/d$ determines the location of the maximum value of the pulse, $v(r) = a + br$ is the pulse front velocity as a function of radial distance r, d is the width of the pulse, $c_1 (> 0)$ and $p (> 0)$ describe the local time dependence of the electric field amplitude, which is largest at ϕ_0, $t_a = (c_2/v_a)(1 - \cos(\phi - \phi_0))$ represents the delay of the pulse from ϕ_0 to other local times, c_2 determines the magnitude of the delay, v_a is the longitudinal speed of the pulse (assumed constant),and r_i is a parameter in the simulation that determines the arrival time of the pulse.

[34] Equation (5) can generally be viewed as a product of three main terms:

[35] (1) E_0, which can be seen as a weight of the magnitude of the pulse and can be manipulated to vary the absolute value of the amplitude of the pulse;

[36] (2) $(1 + c_1 \cos(\phi - \phi_0))^p$ is the term that describes the local time dependence of the electric field amplitude and ensures largest values of the pulse at ϕ_0; and

[37] (3) the exponential term $e^{(-\xi^2)} = e^{[r - r_i + v(r)(t - t_a)]/d}$ that is responsible for the inward propagation of the pulse front. The exponential term determines the shape and the speed of the propagation front of the pulse and it is highly dependent of the width of the propagating impulsive electric field.

[38] Figure 4 shows the evolution of the electric and magnetic fields from the pulse at 10, 8, 6, and 4 R_E. The electric and magnetic fields were computed for the pulse with initial amplitude E_0 of 4 mV/m. At 10 R_E, the electric field of the pulse reaches 60 mV/m and the magnetic field is about 220 nT. Already at 6 R_E, the electric field decreases down to 8 mV/m and magnetic field to 30 nT. The relation between the electric and magnetic fields is similar as in *Li et al*. [1998] and *Sarris et al*. [2002]. We introduced a normalization coefficient $A_{E_{\max}} = 1024$ for the electric pulse amplitude since using directly the equation (1) from *Sarris et al*. [2002] gives unrealistic numbers for maximum E_ϕ at midnight [*Ganushkina et al*., 2005]. Following *Sarris et al*. [2002], we used $\phi_0 = 0, c_1 = 1, c_2 = 0.5 R_E, a = 53.15$ km/s, $b = 0.0093$ s^{-1}, $p = 8, v_a = 20$ km/s, $r_i = 100 R_E$, and $d = 4 \cdot 10^7$ m. The magnetic field disturbance from this dipolarization process was obtained from Faraday's law ($\partial \mathbf{B}/\partial t = -\nabla \times \mathbf{E}$). The total fields are always used in the drift velocity calculations.

[39] There are two main input parameters, the amplitudes and the times of pulses, which must be specified, when modeling a storm development with a series of substorm-associated pulses. We launch a pulse at each substorm onset during the period of a modeled storm. The substorm onsets and the peaks have been automatically detected by a routine that locates steep gradients and local maxima in *AL* and *AE* indices [*Amariutei and Ganushkina*, 2012]. The algorithm enables us to launch pulses at every substorm onset, at a precise time. The amplitude of the pulse has been scaled accordingly to the amplitudes of the *AE* peaks. Assuming a baseline value $E_0 = 4$ mV/m for *AE* index of 1000 nT [*Sarris et al*., 2002], we set the ratio of the pulse amplitudes similar to the ratios of the peak values in the *AE* index. Figure 5 shows the *AE* index for the 6–7 November 1997 storm with times of substorm onsets marked by vertical lines and Table 1 presents the times of substorm onsets, corresponding peak magnitudes of the *AE* index, and amplitudes E_0 of the launched pulses.

[40] Figure 6 shows the AE index for the 12–14 June 2005 storm with times of substorm onsets marked by vertical lines and Table 2 presents the times of substorm onsets, corresponding peak magnitudes of the AE index, and amplitudes E_0 of the launched pulses.

[41] It is necessary to mention that after the pulse has gone, there exists a residual magnetic field [*Li et al*., 1998, Figure 1]. This is the magnetic field from the pulse which does not disappear but continues to contribute to the total magnetic field. When a set of pulses is launched, the residual magnetic field causes non-realistic gradients in the total magnetic field and non-realistic behavior of particle trajectories. Therefore, we have introduced a damping mechanism that switches on a decay of the disturbance magnetic field from the pulse with a damping decrement τ. This moment corresponds to the end of the active phase of the pulse. It is determined from the ratio between the magnetic field changes with time $\frac{\partial B}{\partial t}$ (computed from the Maxwell equation $\frac{\partial B}{\partial t} = -\nabla \times \mathbf{E}$), and the magnetic field changes, which provide a decrease of the current intensity of the magnetic field B by a factor of e during the time of $\tau = 15$ min. If this ratio is smaller than 1, then the magnetic field from the pulse starts to decrease as $B(t) = B(t = 0)\exp(-t/\tau)$. The physical interpretation of this procedure is that after becoming more dipolar during the substorm onset, the magnetic field lines should return to their more tail-like configuration during the substorm recovery.

4. Modeling Results: Comparison of Electron Fluxes at Geostationary Orbit with LANL Observations

[42] The output of the IMPTAM modeling was compared to the observed electron fluxes in four energy ranges measured onboard LANL spacecraft by the SOPA instrument for 6–7 November 1997 and 12–14 June 2005 storms. The variability of fluxes observed on LANL is a result of a delicate balance of non-adiabatic acceleration, loss to the magnetopause, and adiabatic changes and variations in MLT. Accurate modeling of observed fluxes is a challenging task and needs to account for all these competing processes. Although we show the comparison for all MLTs, it should be noted that modeled electrons move only by $\mathbf{E} \times \mathbf{B}$ and magnetic drifts with the only loss process of convective outflow on the magnetopause. No other loss processes are taken into account when the modeled electrons come from the plasma sheet and reach the geostationary orbit at other than nightside MLTs. Thus, the most appropriate comparison can be made on the nightside.

4.1. Influence of the Choice of the Electric Field Model

[43] First, we investigated the possible influence of choice of the electric field model on the modeled electron fluxes along the orbits of LANL satellites. Figure 7a shows the measured pitch angle averaged electron fluxes at geostationary orbit by SOPA instrument onboard LANL 1994-084 satellite and

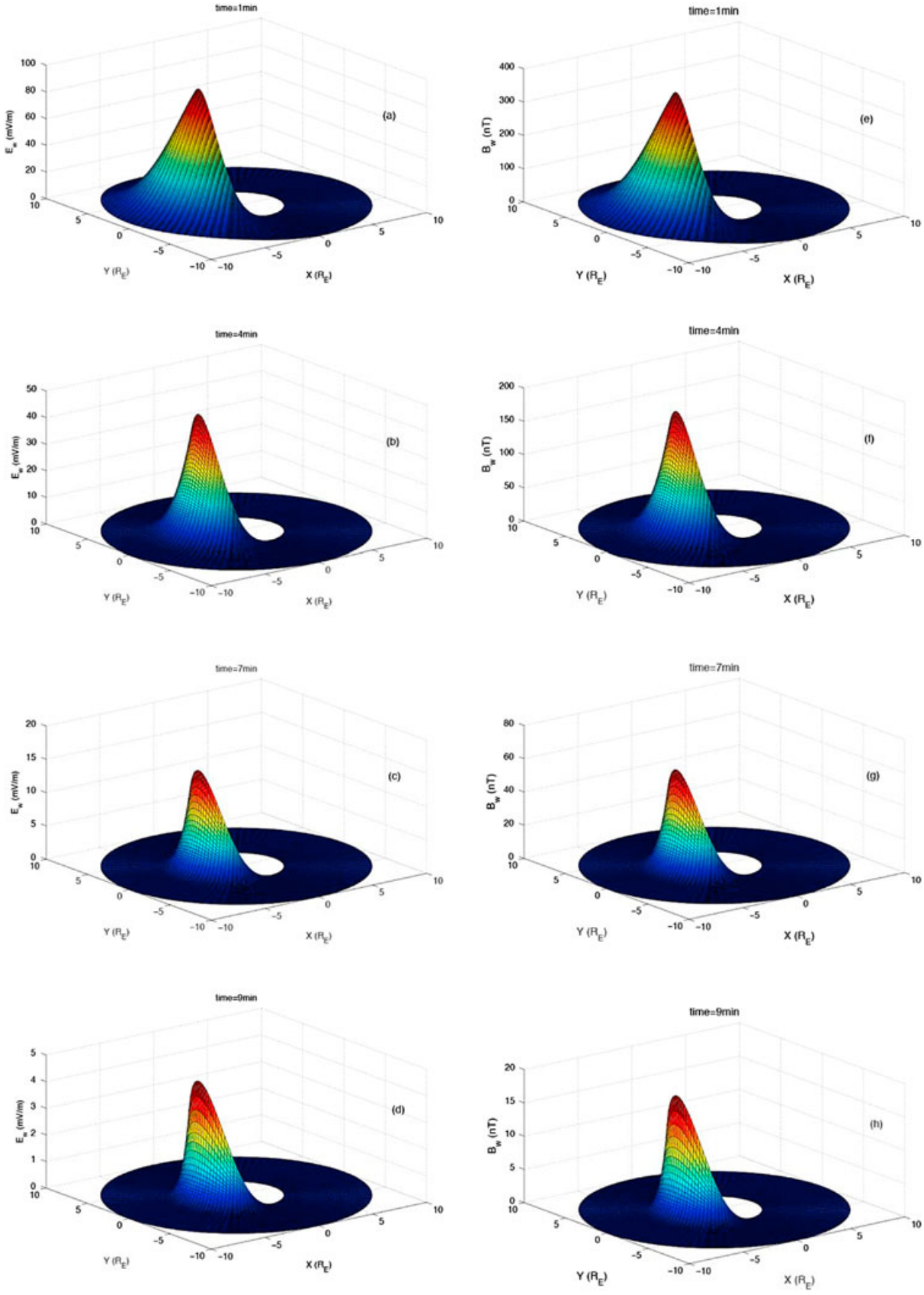

Figure 4. Illustration of the evolution of the electric and magnetic field from the pulse (a and e) coming from 10 R_E, (b and f) decreasing in velocity as it approaches 8 R_E, (c and g) then 6 R_E, and (d and h) arrives to 4 R_E at a considerable reduced amplitude during 10 min. Note that the panels have different Y axis scales.

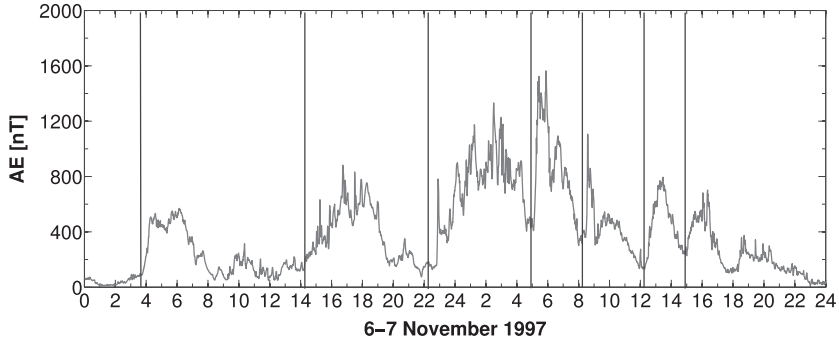

Figure 5. *AE* index for 6–7 November 1997 storm with times of substorm onsets marked by vertical lines.

Table 1. Times of Substorm Onsets, Corresponding Peak Magnitudes of *AE* Index, and Amplitudes E_0 of the Launched Pulses for 6–7 November 1997

UT	*AE* peak, nT	E_0, mV/m
6 November 1997		
0340	580	3
1455	700	4
2255	1350	7
7 November 1997		
0510	1580	8
0820	1100	6
1225	800	4
1500	700	4

Table 2. Times of Substorm Onsets, Corresponding Peak Magnitudes of *AE* Index, and Amplitudes E_0 of the Launched Pulses for 12–13 June 2005

UT	*AE* peak, nT	E_0, mV/m
12 June 2005		
0540	601	3
1319	1023	4
1711	2115	8
2240	1391	5
13 June 2005		
0121	1452	7
0536	1573	6
0816	1183	4
1153	1203	5
1739	959	4

Figure 7d onboard LANL-97A satellite during 6–7 November 1997 storm. Four energy channels are presented: 50–75 keV (black lines), 75–105 keV (pink lines), 105–150 keV (red lines), and 150–225 keV (blue lines). Yellow and blue triangles indicate local noon and midnight, respectively. The LANL SOPA data are in the format of spin-averaged differential fluxes (#/(cm^2*sec* sr keV)). The output from the model is integral flux (#/(cm^2*sec*)) produced by all electrons coming from all directions with energies in those four energy ranges. In order to be able to compare the observed and modeled fluxes more properly, we need to introduce the width of the energy channel and the solid angle 4π. So, the model electron fluxes are in model flux/($4\pi\Delta E$). Figures 7b and 7e present the modeled electron fluxes obtained using IMPTAM by following the electron distribution from 10 R_E to LANL orbits in the combination of the Tsyganenko T96 magnetic field and Volland-Stern electric field models. Figures 7c and 7f present the model electron fluxes obtained with the combination of the Tsyganenko T96 magnetic field and *Boyle et al.* [1997] electric field models.

[44] We start simulations with an empty magnetosphere and allow the model to spin up for 8 h to produce an initial state. We show the modeled fluxes (Figures 7b, 7c, 7e, and 7f) starting from 0800 UT on 6 November. The increase in the modeled fluxes, which occurred at about 1200 UT on 6 November roughly corresponds to the peak in the data at around 1400–1500 UT, when the satellite was close to local midnight. The modeled fluxes are about one order of

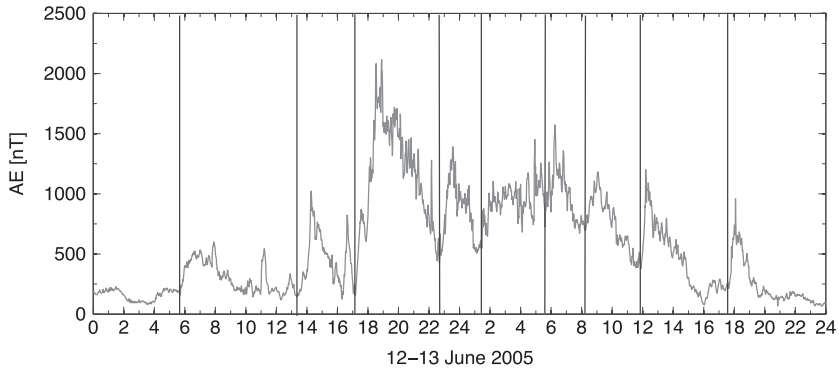

Figure 6. *AE* index for 12–13 June 2005 storm with times of substorm onsets marked by vertical lines.

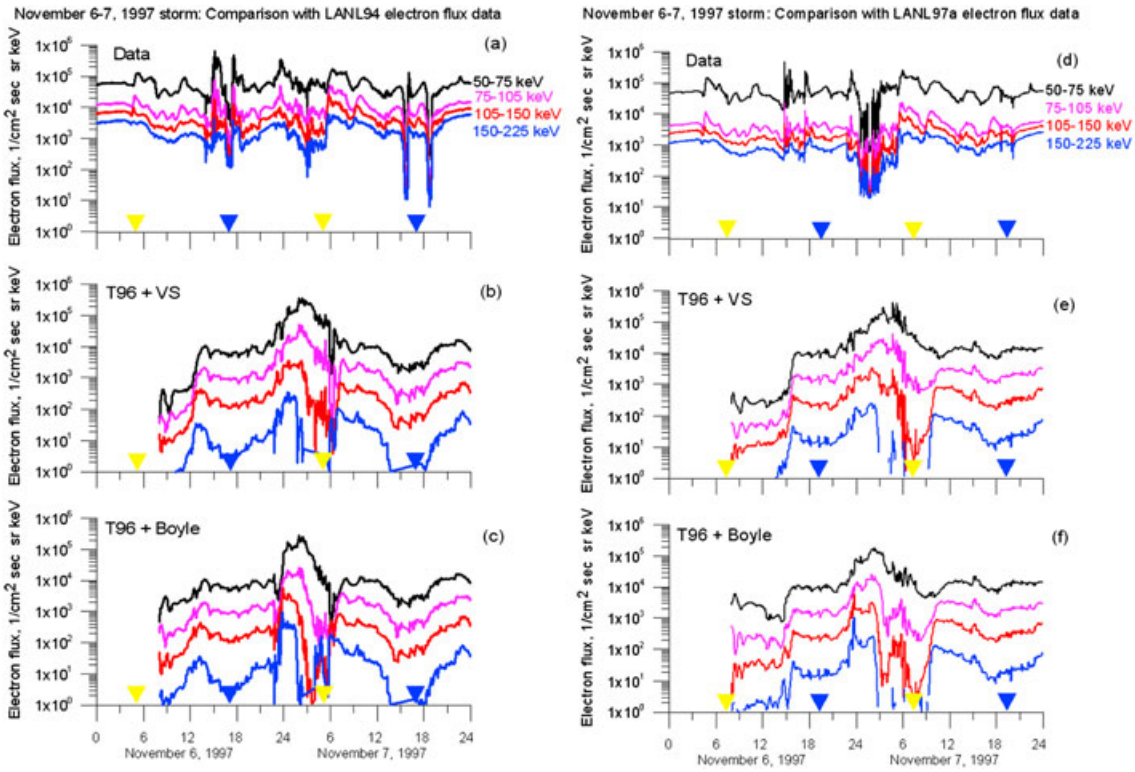

Figure 7. Electron fluxes at geostationary orbit measured by SOPA instrument onboard (a) LANL 1994-084 satellite and (d) LANL-97A satellite during 6–7 November 1997 storm and modeled by IMPTAM in (b and e) Tsyganenko T96 magnetic field and Volland-Stern electric field models and in (c and f) Tsyganenko T96 magnetic field and *Boyle et al*. [1997] electric field models with *Tsyganenko and Mukai* [2003] boundary conditions at 10 R_E. Yellow and blue triangles indicate the local noon and midnight, respectively.

magnitude lower than the observed fluxes during this time (two orders for higher energy electrons with 150–225 keV). When moving toward noon on 7 November, the modeled fluxes show another increase, smooth now, which also has a corresponding peak in the data at about 00 UT 7 November. There is a pronounced decrease in the modeled fluxes at noon with fluxes with energies at 150–225 keV almost dropping to zero. Another drop of the observed fluxes, when the satellite was at midnight around 1800 UT is seen in the modeled fluxes but with different magnitudes. In general, the dynamics of the modeled fluxes follows very approximately the dynamics of the observed fluxes but the magnitudes have one to two orders difference. The combination of models for electric and magnetic fields and boundary conditions used to model the electron fluxes was not sufficiently accurate for IMPTAM to be able to reproduce the fluxes.

[45] The Volland-Stern electric field model used to produce Figure 7b is *Kp*-dependent, and changes in the electric field in the magnetosphere occur every 3 h. Figure 7c presents similar model results but using *Boyle et al*. [1997] electric field model, which depends on the IMF and solar wind parameters, namely, the IMF total magnetic field, clock angle, and solar wind velocity. As can be seen in Figure 7c, the general profiles and magnitudes of the modeled fluxes do not significantly change, when changing from the Volland-Stern to the *Boyle et al*. [1997] electric field model. All features described above are valid for Figures 7e and 7f, where modeled fluxes were compared to the measured ones onboard the LANL-97A satellite.

[46] Similarly to Figure 7, Figure 8 shows the measured electron fluxes at geostationary orbit by SOPA onboard the LANL-01A satellite and onboard the LANL-02A satellite together with modeling results but for 12–14 June 2005 storm event starting at 0800 UT on 12 June. Similarly to the previous storm, there is one order of magnitude difference between the observed and modeled fluxes and two orders for electrons with energies of 150–225 keV that can be clearly seen in Figures 8b and 8c. The increase of fluxes at all energies seen at 1800 UT on 12 June can be also seen in the modeled fluxes when using both Volland-Stern (Figure 8b) and *Boyle et al*. [1997] (Figure 8c) electric field models. The drop in the observed fluxes around 2000 UT appears in the modeled fluxes closer to the end of the day of 12 June. Modeled fluxes maintain lower values longer, slowly recovering by 0500 UT on 13 June. A drop in the modeled fluxes around 1000 UT and an increase in all modeled fluxes at the end of 14 June are observable in the simulation results near noon but such a pronounced drop is not observable in the measured data. In general, using the *Boyle et al*. [1997] electric field model instead of Volland-Stern did not change the pattern of the modeled fluxes much. All features described above are valid for Figures 8e and 8f, where modeled fluxes were compared to the measured ones onboard LANL02A.

4.2. Influence of the Choice of the Magnetic Field Model

[47] Next, we investigated the possible influence of the magnetic field choice on the modeled electron fluxes along the orbits of the LANL satellites. Figure 9a shows the

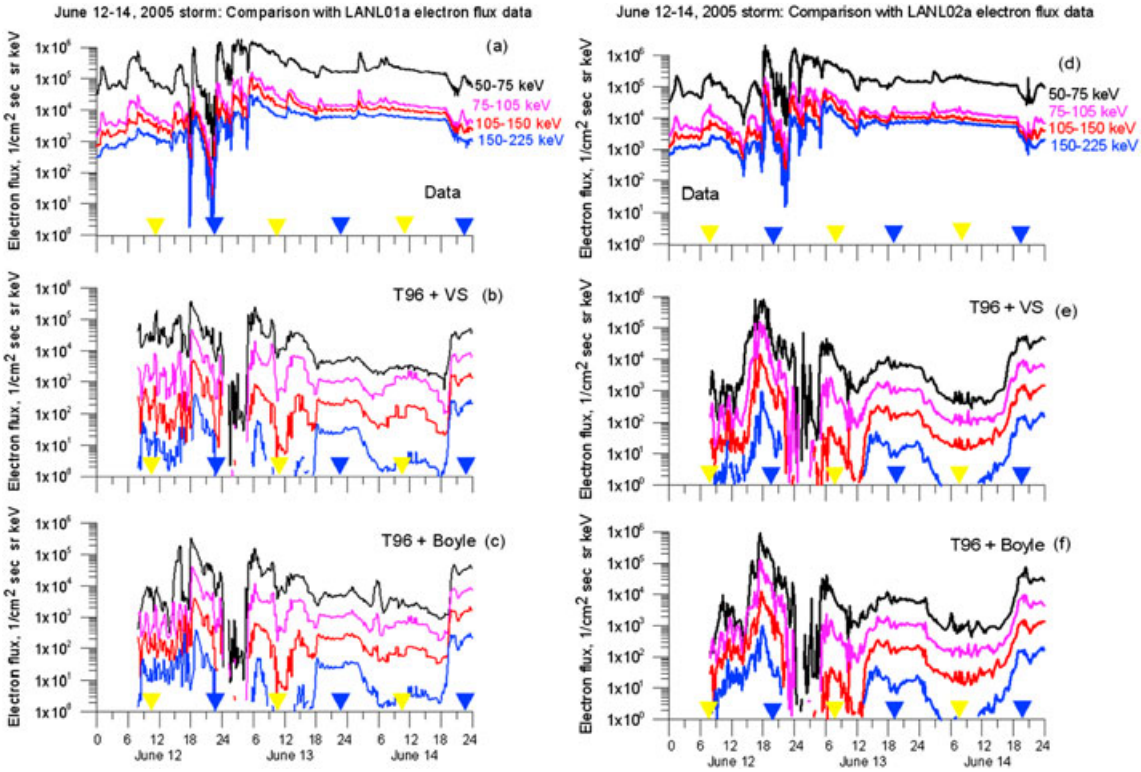

Figure 8. Similar to Figure 7 but for 12–14 June 2005 storm when electron fluxes at geostationary orbit were measured by SOPA instrument onboard LANL-01A and LANL-02A satellites.

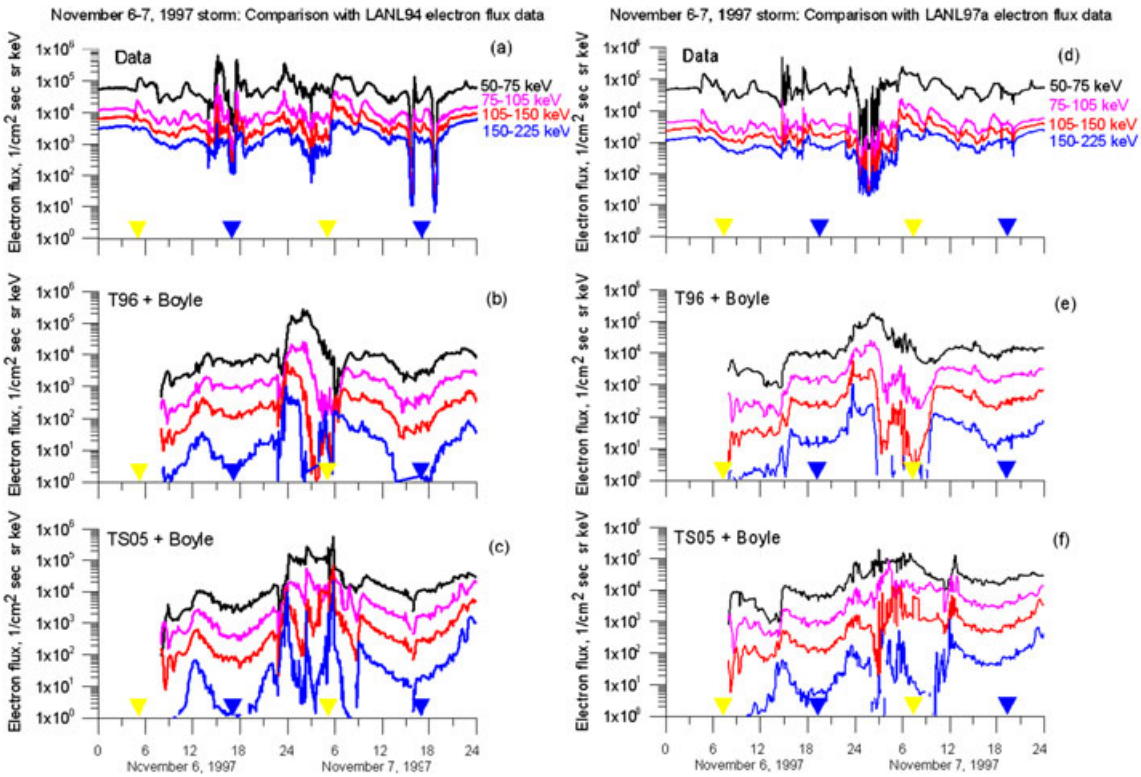

Figure 9. Electron fluxes at geostationary orbit measured by SOPA onboard (a) LANL 1994-084 and (d) LANL-97A during 6–7 November 1997 storm and modeled by IMPTAM in (b and e) the Tsyganenko T96 magnetic field and *Boyle et al.* [1997] electric field models and in (c and f) the Tsyganenko and Sitnov TS05 magnetic field and *Boyle et al.* [1997] electric field models with *Tsyganenko and Mukai* [2003] boundary conditions at 10 R_E. Yellow and blue triangles indicate the local noon and midnight, respectively.

measured electron fluxes at geostationary orbit by SOPA onboard LANL 1994-084 and Figure 9d onboard LANL-97A during 6–7 November 1997 storm. Figures 9b and 9e present the modeled electron fluxes obtained by following the electron distribution from 10 R_E in the plasma sheet to the LANL orbits in the combination of the Tsyganenko T96 magnetic field and *Boyle et al*. [1997] electric field models. Similarly as was mentioned above, we compare the observed electron fluxes with the modeled ones, where the width of the energy channel and the solid angle are taken into account. Figures 9c and 9f present the model electron fluxes obtained with the combination of the *Tsyganenko and Sitnov* [2005] TS05 magnetic field and *Boyle et al*. [1997] electric field models. Similarly to the previously shown results, we present the modeled fluxes starting from 0800 UT on 6 November so that the magnetosphere is filled with particles after the beginning of our IMPTAM modeling with the empty magnetosphere.

[48] Comparison between Figures 9b and9 c reveals that changing from T96 magnetic field model, which is dependent on *Dst*, IMF and solar wind parameters, to the TS05 model, where each source was parameterized by solar wind and IMF integrals from the moment in time when the storm started, does not significantly change the magnitudes of the modeled fluxes. The modeled electron fluxes are one order of magnitude lower than the observed ones for the electron energies from 50 to 150 keV, and about two orders lower for the high-energy electrons (150–225 keV). The profiles of fluxes (Figure 9c), when TS05 model was used, are closer to the observed ones, showing more changes, although not dramatic. The nightside variations of fluxes observed at around 1500–1800 UT on 6 November are reflected in the modeled fluxes as an increase in all energy ranges around 1200–1500 UT. The first observable difference is the higher values for fluxes and more variations at around 0300–0600 UT on 7 November, when the LANL94 satellite was near noon. The flux decrease observed at around 1800 UT on 7 November, when the satellite was near midnight, is present in the model fluxes (Figures 9b and 9c). Comparison with the electron fluxes observed onboard LANL-97A shows similar features as described above.

[49] Similarly to Figure 9, Figure 10 shows the measured electron fluxes at geostationary orbit by SOPA onboard LANL-01A (Figure 10a) and onboard LANL-02A (Figure 10d) together with modeling results but for 12–14 June 2005 storm event. For this storm, using the TS05 model instead of the T96 model resulted in rather different modeled fluxes. The striking signature is the large increase of the modeled fluxes when using TS05 around noon in the middle of 12 June (Figure 10c), which is not seen in the data and was not obtained using the T96 model (Figure 10b). Later increases and dropouts of the modeled fluxes have rather different timing compared to the data and when T96 model was used. The same pattern can be seen when comparing with LANL-02A data (Figures 10e and 10f). In general, simulations using the TS05 model resulted in the modeled electron fluxes much less resembling observations that simulations using the T96 model.

4.3. Role of Substorm-Associated Electromagnetic Fields

[50] In addition to the large-scale electric and magnetic fields, we launched several electromagnetic pulses at substorm onsets determined as sharp increases in the AE index (Figure 5) with amplitudes given in Table 1 when modeling the 6–7

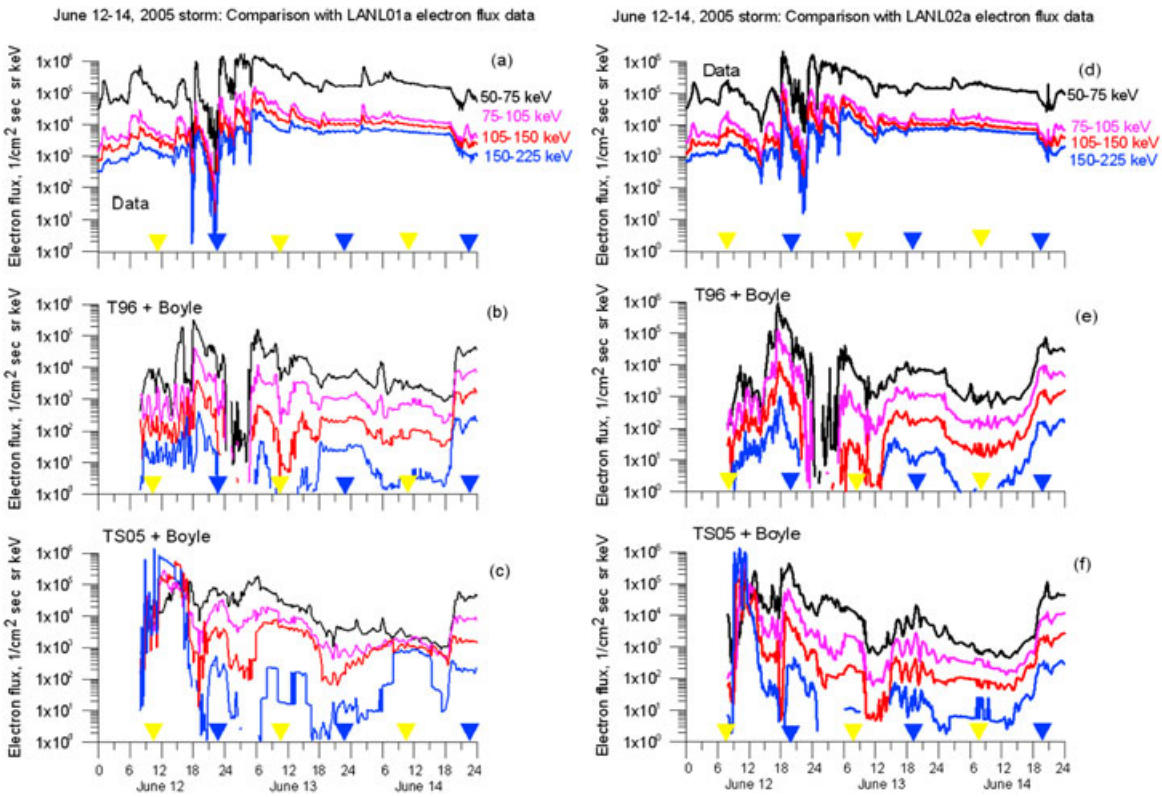

Figure 10. Similar to Figure 9 but for 12–14 June 2005 storm when electron fluxes at geostationary orbit were measured by SOPA onboard LANL-01A and LANL-02A.

November 1997 storm event. Figure 11 presents the electron fluxes at geostationary orbit (Figure 11a) measured by SOPA onboard LANL 1994-084 during the 6–7 November 1997 storm and modeled by IMPTAM where the width of the energy channel and the solid angle are taken into account with *Tsyganenko and Mukai* [2003] boundary conditions at 10 R_E in the T96 magnetic field and *Boyle et al.* [1997] electric field models (Figure 11b), with the addition of several substorm-associated electromagnetic pulses (Figure 11c) at substorm onsets (Figure 5), in the Tsyganenko and Sitnov TS05 magnetic field and *Boyle et al.* [1997] electric field models (Figure 11d), and with the addition of several substorm-associated electromagnetic pulses (Figure 11e) at substorm onsets (Figure 5).

[51] As can be seen when comparing Figures 11b and 11c, the introduction of seven pulses during the modeled storm event did not change the modeled electron fluxes significantly, when the T96 and *Boyle et al.* [1997] models were used. The main differences include a sharp increase of the modeled fluxes at all energies in the beginning of the modeling on 6 November around 0400–0500 UT, which corresponds to the initiation of the first pulse at 0340 UT (see Table 1). LANL 1994-084 was near noon at that time. Since pulses are coming from the nightside and decrease toward dawn and dusk, their influence should be seen most on the nightside. When the satellite moved to the nightside around 1700 UT, no pulses were launched, and the influence of the second pulse at 1455 UT has already diminished. Similar features can be seen in Figures 11d and 11e, when the TS05 model was used for the magnetic field instead of T96.

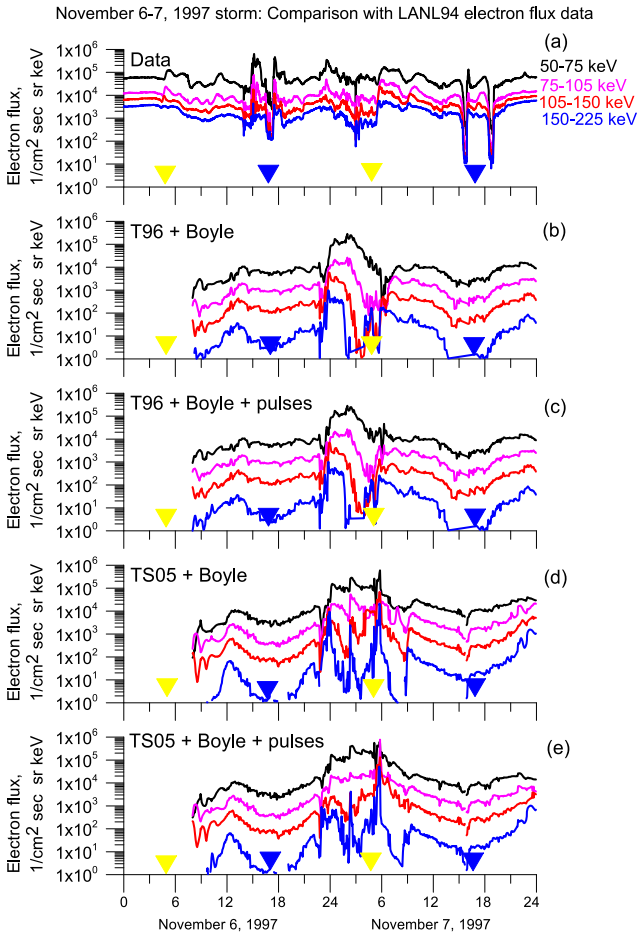

Figure 11. Electron fluxes at geostationary orbit measured by SOPA onboard (a) LANL 1994-084 during 6–7 November 1997 storm and modeled by IMPTAM in (b) T96 magnetic field and *Boyle et al.* [1997] electric field models, (c) with addition of several substorm-associated electromagnetic pulses at substorm onsets (Figure 5), (d) in Tsyganenko and Sitnov TS05 magnetic field and *Boyle et al.* [1997] electric field models, and (e) with addition of several substorm-associated electromagnetic pulses at substorm onsets (Figure 5) with *Tsyganenko and Mukai* [2003] boundary conditions at 10 R_E. Yellow and blue triangles indicate the local noon and midnight, respectively.

[52] During the 12–14 June 2005 storm, the difference between the modeled fluxes with and without the influence of the launched pulses is more evident (see Figures 12b and 12c, where T96 and *Boyle et al.* [1997] models were used). From 0600 to 1800 UT on 12 June, when LANL-01A was on the dayside, adding pulses resulted in about one order higher electron fluxes for all energies. We can see (Figure 12c) the increases in the modeled fluxes around 0600 UT, 1400 UT, and 1700 UT, which correspond to the pulses launched at about those times (Figure 6 and Table 2). In the beginning of

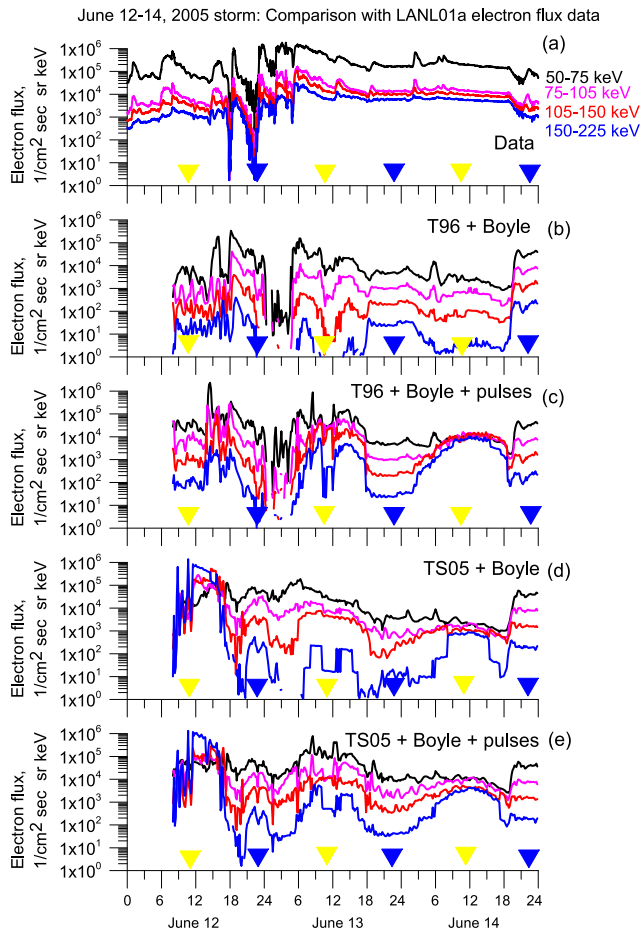

Figure 12. Similar to Figure 11 but for 12–14 June 2005 storm when electron fluxes at geostationary orbit were measured by SOPA onboard LANL-01A.

13 June, LANL-01A moved to the nightside and there is an evident increase in the modeled fluxes around 0300 UT (10^1 #/(cm^{2}sec sr keV) instead of almost 10^0 for electrons with energies of 150–225 keV, 10^2 #/(cm^{2}sec sr keV) instead of almost 10^0 #/(cm^{2}sec sr keV) for electrons with energies of 105–150 keV, 10^3 #/(cm^{2}sec sr keV) instead of 10^1 for electrons with energies of 75–105 keV and 10^4 #/(cm^{2}sec sr keV) instead of 10^2 for electrons with energies of 50–75 keV). During that time, two pulses were launched at 2240 UT on 12 June and 0121 UT on 13 June. Another rather significant difference can be seen around 1200 UT on 13 June, when LANL-01A came back to the dayside. Electron fluxes modeled with the influence of the pulses do not show the drop (Figure 12c), which was seen when using just the T96 and *Boyle et al.* [1997] models (Figure 12b) and was not seen in the data (Figure 12a). The last feature is the increased fluxes around 1200 UT on 14 June during the storm recovery phase, when LANL-01A was on the dayside. Fluxes stayed increased on the dayside as was on 13 June. The addition of pulses, when using the TS05 magnetic field model (Figure 12e), shows similar flux increases associated with the launching times of pulses (Figure 6 and Table 2) compared to fluxes when the T96 model was used (Figure 12d). As before, using the TS05 model with pulses resulted in the modeled electron fluxes less close to the observed ones than did the fluxes using the T96 model.

4.4. Role of Radial Diffusion

[53] In addition to drifts, we investigated if radial diffusion (equations (3) and (4)) has any influence on the modeled electron fluxes. Although transport via convective and inductive electric fields is expected to dominate at electron energies of a few tens of keV, at higher energies of a few hundred keV transport by radial diffusion should become more important. Since the agreement between our model and data becomes poorer at higher energies, here we investigate whether radial diffusion is capable of substantially increasing high energy fluxes. We applied the radial diffusion equation (3) for a range of μ values between 0.006 and 6 keV/nT. At $L = 10$, this corresponds to energies of 0.12–120 keV (assuming a magnetic field of 20 nT) rising to 0.3–300 keV (assuming 50 nT) at $L = 6.6$. The diffusion coefficients given by *Brautigam and Albert* [2000] were extrapolated to $L = 10$ using the same equation, which means that radial diffusion is very large at larger L-shells. Thus, our results may only overestimate the effects of transport by radial diffusion. Figure 13

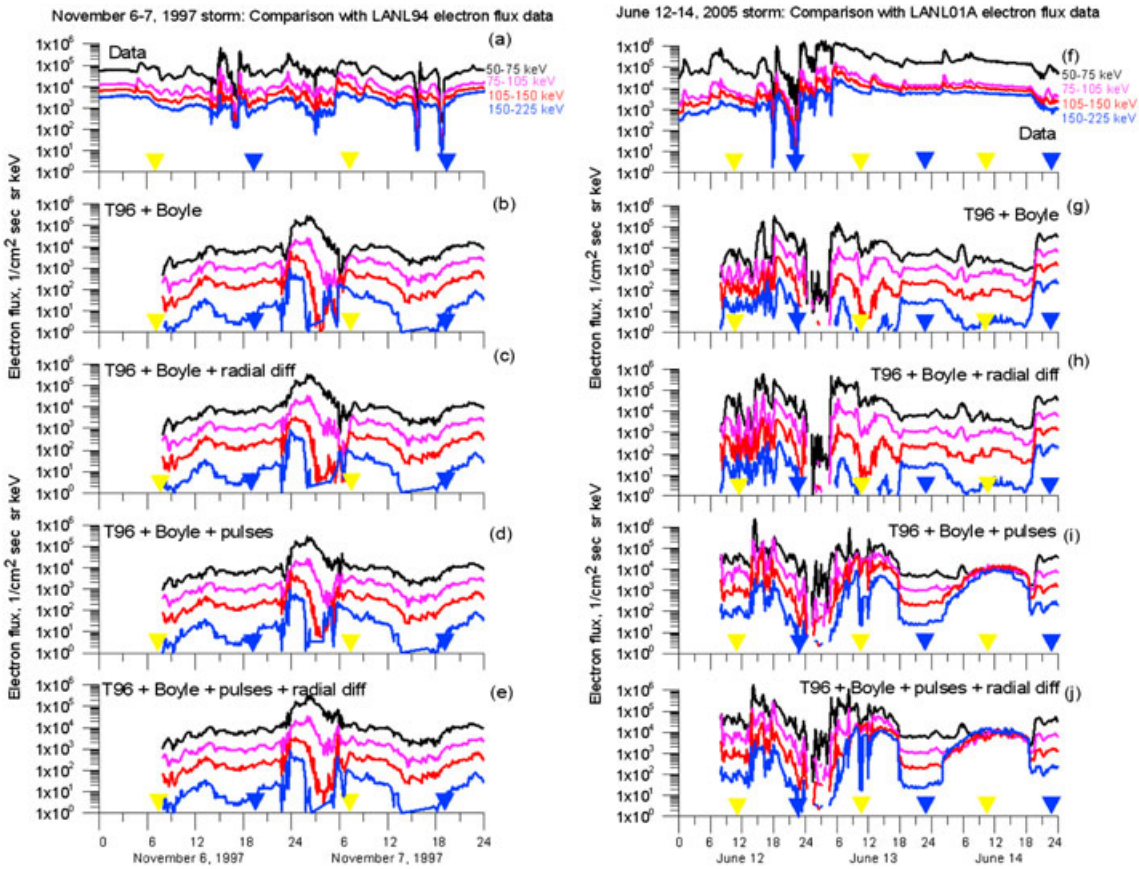

Figure 13. Electron fluxes at geostationary orbit (a) measured by SOPA onboard LANL 1994-084 during 6–7 November 1997 storm together with modeled fluxes when different combination of electromagnetic fields and transport processes were used, such as (b) T96 and *Boyle et al.* [1997] models, (c) T96 and *Boyle et al.* [1997] models with addition of radial diffusion by equations (3) and (4), (d) T96 and *Boyle et al.* [1997] models with addition of several substorm-associated electromagnetic pulses at substorm onsets (Figure 5), and (e) T96 and *Boyle et al.* [1997] models with addition of pulses at substorm onsets and radial diffusion. Figures 13f–13j present similar results but for comparison between the modeled electron fluxes and observed onboard LANL-01A during 12–14 June 2005 storm.

shows the electron fluxes at geostationary orbit (Figure 13a) measured by SOPA onboard LANL 1994-084 during the 6–7 November 1997 storm together with modeled fluxes where the width of the energy channel and the solid angle are taken into account when different combination of electromagnetic fields and transport processes were used, such as T96 and *Boyle et al*. [1997] models (Figure 13b), T96 and *Boyle et al*. [1997] models with addition of radial diffusion by equations (3) and (4) (Figure 13c), T96 and *Boyle et al*. [1997] models with addition of several substorm-associated electromagnetic pulses (Figure 13d) at substorm onsets (Figure 5), and T96 and *Boyle et al*. [1997] models with addition of pulses at substorm onsets and radial diffusion (Figure 13e). Figures 13f–13j present similar results for comparison between the modeled electron fluxes and observed onboard LANL-01A during the 12–14 June 2005 storm. It can be clearly seen that the addition of radial diffusion, with or without the combination of pulses, does not produce any significant influence on the modeled fluxes.

5. Discussion and Conclusions

[54] We investigated the low energy (50–250 keV) electron transport and acceleration from the plasma sheet to geostationary orbit. This low-energy electron population is critically important for the radiation belt dynamics as it can serve as a seed population for the high-energy MeV particles and can also provide energy for chorus waves. We specifically studied the role of large-scale convection, choice of the background magnetic field model, influence of the substorm-associated electromagnetic fields, and radial diffusion processes on the modeled electron fluxes at geostationary orbit. We used the Inner Magnetosphere Particle Transport and Acceleration Model (IMPTAM) [*Ganushkina et al*., 2001; *Ganushkina et al*., 2005, 2006, 2012b] with the boundary at $10\,R_E$, where we set boundary conditions for the electrons based on Tsyganenko and Mukai [*Tsyganenko and Mukai*, 2003] model. We modeled two moderate storm events, which occurred on 6–7 November 1997 and 12–14 June 2005. The output of the IMPTAM modeling was compared to the observed electron fluxes in four energy ranges measured onboard LANL spacecraft by SOPA.

[55] As a result of the comparison of modeled fluxes to the LANL observations, we found that our first modeling results can approximately capture the general dynamics of the observed fluxes for both storms. Increases and dropouts of the modeled fluxes reproduce some of the trends seen in observations (see, for example, Figures 7 and 8); however, the timing of fast changes was not often captured. The main difference was in the magnitudes of the modeled fluxes which were one (two) order(s) smaller than the observed ones for 50–150 keV (150–225 keV) electrons, respectively. This difference of one/two orders of magnitude cannot be explained by inaccuracy of the field models, since it was present for all combinations of electric and magnetic field models. One possible explanation for the underestimates of the observed fluxes is that the boundary conditions we used at $10\,R_E$ were adapted from the empirical model derived from Geotail data by *Tsyganenko and Mukai* [2003] for ions. We used the same number density as for ions and for electron temperature we just set $Te/Ti = 0.2$. According to recent studies based on Geotail data analysis [*Wang et al*., 2011], the ratio *Te/Ti* can vary during disturbed conditions. Furthermore, there was no MLT-dependence in the kappa distribution with n and T parameters from *Tsyganenko and Mukai* [2003] model, which is also not the case according to the observations [*Wang et al*., 2011]. Thus, the model we used for boundary conditions has a number of limitations. However, it is currently the best analytical model that can be used for time-dependent boundary conditions at $10\,R_E$ in the plasma sheet. Use of more accurate analytical models for boundary fluxes may significantly improve the simulation results.

[56] Another important issue is the absence of the loss processes for modeled electrons to the atmosphere due to the resonant pitch-angle scattering by chorus waves, which can have an influence at distances from 10 to $6.6\,R_E$ in the plasma sheet. *Shprits et al*. [2007] developed parameterization for the loss of electrons with energies of 100 keV and above to the atmosphere due to the resonant pitch-angle scattering by chorus waves. Chorus waves are excited by the anisotropy of ring current electrons, which are injected into the inner magnetosphere during the periods of enhanced convection [*Meredith et al*., 2001; *Lyons et al*., 2005]. Interactions with chorus waves lead to electron pitch angle scattering into the loss cone, where they are removed within a quarter bounce time [*Horne and Thorne*, 2003]. Future modeling should include loss process similar to *Shprits et al*. [2007] and/or *Chen et al*. [2005]. We considered only convection outflow as a loss process, when following the low-energy electrons from $10\,R_E$ to $6.6\,R_E$ on purpose to study how the convection and substorm-associated fields can bring plasma sheet electrons inward. Introducing the loss processes due to wave-particle interactions is important for low-energy electrons and will be part of our future study.

[57] Changing of the global electric field model used in IMPTAM from the *Kp*-dependent Volland-Stern model to the *Boyle et al*. [1997] model, which depends on the IMF and solar wind parameters, did not result in significant changes of the general profiles and magnitudes of the modeled fluxes. There is not much difference between the equipotential contours given by these two convection models at the distances from 10 to $6.6\,R_E$ in the plasma sheet. The main differences are present inside $6.6\,R_E$ (see, for example, the analysis done by *Pierrard et al*. [2008]). For the background magnetic field, using the TS05 model resulted in the modeled electron fluxes much less close to the observed ones than using the T96 model. TS05 model was constructed by using the data only for 37 storms with $Dst < -65$ nT that occurred between October 1996 and November 2000 [*Tsyganenko et al*., 2003]. As in the previous versions, the model magnetic field is a superposition of the magnetic fields from several modules, which represent the magnetospheric current systems. As was shown by *Ganushkina et al*. [2012a], the different modules can occupy the same space and sometimes produce nonphysical configurations (e.g., thin tail current piercing thick ring current region). Thus, particle trajectories depend on the magnetic field models that are used and special care should be taken when the modeling results are interpreted. IMPTAM can take into account the self-consistency of the magnetic field by calculating the magnetic field produced by the model currents and feeding it back to the background magnetic field. It is necessary to be careful when calculating a self-consistent magnetic field using a realistic model

magnetic field such as Tsyganenko models. These models contain the prescribed ring and near-Earth tail currents. If they are used together with calculations of the induced magnetic field to trace particles in them, the obtained results will be incorrect [*Ganushkina*, 2011]. To be accurate, it is necessary to remove the model ring and near-Earth tail currents from the background magnetic field model and consider self-consistent calculations of the magnetic field. At the distances from 10 to 6.6 R_E, the effect of the self-consistent magnetic field is expected to be small. This subject will be for future study.

[58] The substorm-associated electromagnetic fields play a role in the electron transport and acceleration from the plasma sheet to the inner magnetosphere and they must be taken into account when modeling the electron population. As can be seen in Figures 11 and 12, the increases in the modeled fluxes correspond to the pulses launched at about those times (Figures 5 and 6, and Tables 1 and 2). The increase can be as large as two orders of magnitude (Figures 12b and 12c). Pulses are launched on the nightside, in the representation by *Sarris et al*. [2002] used here, they move rather fast (less than 10 min). The modeled fluxes along LANL orbits at different MLTs may not show the influence of the launched pulses.

[59] At the same time, as the results shown in the present paper are our first attempts to take into account the smaller-scale fields associated with substorms in addition to large-scale fields, further investigation and development of the employed model for pulses is necessary. There have been several studies where a similar representation of electromagnetic pulses by *Li et al*. [1998] or *Sarris et al*. [2002] were used and good agreement with the observed dispersionless electron injections at geostationary orbit was obtained [*Ingraham et al*., 2001; *Li et al*., 2003; *Mithaiwala and Horton*, 2005; *Liu et al*., 2009]. However, previous studies considered individual substorms or injections. In our study, we launch several pulses during each storm event, since several substorms occur during storms. Stormtime substorms can be very different from the isolated substorms [*Pulkkinen et al*., 2005], and the pulse model needs to be modified. For example, the linear dependence of the pulse's velocity on R_E and the arrival time of the pulse as the pulse would not stop propagating at the specified distance must be modified to fit observations [*Ohtani*, 1998; *Sergeev et al*., 1998; *Reeves et al*., 1996]. Another two parameters that might also be critical in capturing the effectiveness of a substorm pulse in transporting particles are the azimuthal extent and impact location, which were discussed in *Sarris and Li* [2005].

[60] The addition of radial diffusion practically did not change the modeled electron fluxes. Radial diffusion is one of several means of accelerating radiation belt electrons to their observed relativistic energies, and is sometimes used as the only acceleration method to describe the electron flux variations [*Barker et al*., 2005]. Similar to any of the diffusion processes, radial diffusion requires a gradient in at least one coordinate and multiple displacements of the particles of this coordinate. In the case of radial diffusion, there must be a radial gradient in phase space density. At the considered distance from 10 to 6.6 R_E in the plasma sheet, the distribution function produced by convection with neglect of losses is rather flat, so no significant influence from radial diffusion is expected.

[61] The electron fluxes in higher energy ranges, such as 150–225 keV, were almost never high enough as a result of our modeling in all combinations of models. Addition of pulses and radial diffusion also did not produce significant high energy fluxes. This can mean that the assumptions in IMPTAM and combination of models and boundary conditions used to model the electron fluxes were not sufficiently correct for IMPTAM to be able to reproduce higher energy fluxes. There can be an internal acceleration source due to wave-particle interactions that contributes at this energy. Global simulation results also found that additional acceleration is required [*Varotsou et al*., 2005; *Horne et al*., 2006; *Albert et al*., 2009; *Fok et al*., 2008; *Shprits et al*., 2009]. *Shprits et al*. [2009] suggested that electrons at energies of tens of keVs are injected inside geostationary orbit where they are accelerated to MeV energies. This process will create peaks in PSD at *L*-shells of 4–5. These electrons accelerated locally to MeVs will then diffuse inward and outward. During the outward transport, particles will be decelerated. This process may explain the origin of energetic particles at geostationary orbit.

[62] We must stress once again that although we show the comparison between the modeled and observed fluxes at all MLTs, the most appropriate comparison can be made only on the nightside. No loss processes due to wave-particle interactions were taken into account when the modeled electrons come from the plasma sheet, enter the inner magnetosphere, and reach the geostationary orbit at other than nightside MLTs. Keeping the points discussed above in mind, the conclusions are as follows:

[63] 1. Transport of plasma sheet electrons from 10 R_E in the plasma sheet to geostationary at 6.6 R_E during storm times is due to the large-scale convection in combination with substorm-associated impulsive fields. The addition of radial diffusion has no significant influence on the modeled electron fluxes.

[64] 2. The modeled electron fluxes are one (two) order(s) smaller than the observed ones for 50–150 keV (150–225 keV) electrons, respectively, which indicate the inaccuracy of electron boundary conditions. The loss processes due to wave-particle interactions should be considered. Modeling with current version of IMPTAM and combination of models and boundary conditions used to model the electron fluxes were not sufficiently correct.

[65] 3. The choice of the large-scale convection electric field model does not significantly influence on the modeled electron fluxes, since the equipotential contours given by the Volland-Stern and Boyle et al. [1997] models are quite similar at the distances from 10 to 6.6 R_E in the plasma sheet. The main differences are present inside 6.6 R_E. Using the TS05 model for the background magnetic field instead of the T96 model resulted in the modeled electron fluxes much less close to the observed ones due to specific features of the TS05 model.

[66] 4. The increase in modeled electron fluxes can be as large as three orders of magnitude when substorm-associated electromagnetic fields are taken into account. Modifications of the pulse model by Sarris et al. [2002] used here are needed, especially related to the pulse front velocity and arrival time.

[67] **Acknowledgments.** We thank OMNIWEB data center for IMF and solar wind parameter data, World Data Center C2 for Geomagnetism, Kyoto, for the provisional *AE*, *Kp*, and *SYM-H* indices data. We would like to acknowledge the Los Alamos National Laboratory Space Physics and Applications Group for the data from LANL MPA and SOPA instruments. The research leading to these results has received funding from the European Union Seventh Framework Programme (FP7/2007-2013) under grant agreement 262468. N. Ganushkina gratefully acknowledges the support of part of this work by NASA and NSF grants. We thank R. Horne for very valuable comments and suggestions.

References

Aggson, T. L., J. P. Heppner, and N. C. Maynard (1983), Observations of large magnetospheric electric fields during the onset phase of a substorm, *J. Geophys. Res.*, *88*(A5), 3981–3990, doi:10.1029/JA088iA05p03981.

Albert, J. M., N. P. Meredith, and R. B. Horne (2009), Three-dimensional diffusion simulation of outer radiation belt electrons during the October 9, 1990, magnetic storm, *J. Geophys. Res.*, *114*, A09214, doi:10.1029/2009JA014336.

Amariutei, O. A., and N. Yu. Ganushkina (2012), On the prediction of the auroral westward electrojet index, *Ann. Geophys.*, *30*, 841–847, doi:10.5194/angeo-30-841-2012.

Angelopoulos, V., W. Baumjohann, C. F. Kennel, F. V. Coroniti, M. G. Kivelson, R. Pellat, R. J. Walker, H. Luhr, and G. Paschmann (1992), Bursty bulk flows in the inner central plasma sheet, *J. Geophys. Res.*, *97*(A4), 4027–4039, doi:10.1029/91JA02701.

Baker, D. N., J. B. Blake, L. B. Callis, R. D. Belian, and T. E. Cayton (1989), Relativistic electrons near geostationary orbit: Evidence for internal magnetospheric acceleration, *Geophys. Res. Lett.*, *16*(6), 559–562, doi:10.1029/GL016i006p00559.

Bame, S. J., D. J. McComas, M. F. Thomsen, B. L. Barraclough, R. C. Elphic, J. P. Glore, J. T. Gosling, J. C. Chavez, E. P. Evans, and F. J. Wymer (1993), Magnetospheric plasma analyzer for spacecraft with constrained resources, *Rev. Sci. Instr.*, *64*, 1026.

Barker, A. B., X. Li, and R. S. Selesnick (2005), Modeling the radiation belt electrons with radial diffusion driven by the solar wind, *Space Weather*, *3*, S10003, doi:10.1029/2004SW000118.

Baumjohann, W., G. Paschmann, and H. Luhr (1990), Characteristics of high-speed ion flows in the plasma sheet, *J. Geophys. Res.*, *95*(A4), 3801–3809, doi:10.1029/JA095iA04p03801.

Belian, R. D., G. R. Gisler, T. Cayton, and R. Christensen (1992), High-*Z* energetic particles at geosynchronous orbit during the great solar proton event series of October 1989, *J. Geophys. Res.*, *97*, 16,897.

Birn, J., A. V. Artemyev, D. N. Baker, M. Echim, M. Hoshino, and L. M. Zelenyi (2012), Particle acceleration in the magnetotail and aurora, *Space Sci. Rev.*, *173*(1–4), 49–102.

Birn, J., M. F. Thomsen, J. E. Borovsky, G. D. Reeves, D. J. McComas, and R. D. Belian (1997), Characteristic plasma properties during dispersionless substorm injections at geosynchronous orbit, *J. Geophys. Res.*, *102* (A2), 2309–2324, doi:10.1029/96JA02870.

Birn, J., M. F. Thomsen, J. E. Borovsky, G. D. Reeves, D. J. McComas, R. D. Belian, and M. Hesse (1998), Substorm electron injections: Geosynchronous observations and test particle simulations, *J. Geophys. Res.*, *103*(A5), 9235–9248, doi:10.1029/97JA02635.

Boyle, C., Reiff, P., and Hairston, M., (1997) Empirical polar cap potentials, *J. Geophys. Res.*, *102*(A1), 111–125.

Borovsky J. E., M. F. Thomsen, R. C. Elphic, T. E. Cayton, and D. J. McComas (1998), The transport of plasma sheet material from the distant tail to geosynchronous orbit, *J. Geophys. Res.*, *103*, 20,297–20,331.

Brautigam, D. H., and J. M. Albert (2000), Radial diffusion analysis of outer radiation belt electrons during the 9 October 1990 magnetic storm, *J. Geophys. Res.*, *105*, 291.

Cattell, C. A., and F. S. Mozer (1984), Substorm electric fields in the Earth's magnetotail, in Magnetic Reconnection in Space and Laboratory Plasmas, Geophys. Monogr. Ser., vol. *30*, edited by E. W. Hones Jr., pp. 208–215, AGU, Washington, D.C.

Cayton, T. E., R. D. Belian, S. P. Gary, T. A. Fritz, and D. N. Baker (1989), Energetic electron components at geosynchronous orbit, *Geophys. Res. Lett.*, *16*(2), 147–150, doi:10.1029/GL016i002p00147.

Chen, M. W., M. Schulz, P. C. Anderson, G. Lu, G. Germany, and M. Wüest (2005), Storm time distributions of diffuse auroral electron energy and X-ray flux: Comparison of drift-loss simulations with observations, *J. Geophys. Res.*, *110*, A03210, doi:10.1029/2004JA010725.

Christon, S. P., D. J. Williams, D. G. Mitchell, L. A. Frank, and C. Y. Huang (1989), Spectral characteristics of plasma sheet ion and electron populations during undisturbed geomagnetic conditions, *J. Geophys. Res.*, *94*(A10), 13,409–13,424, doi:10.1029/JA094iA10p13409.

Elkington, S. R., M. Wiltberger, A. A. Chan, and D. N. Baker (2004), Physical models of the geospace radiation environment, *J. Atmos. Sol.-Terr. Phys.*, *66*, 1371–1387, doi:10.1016/j.jastp.2004.03.023.

Friedel, R. H. W., H. Korth, M. G. Henderson, M. E. Thomsen, and J. D. Scudder (2001), Plasma sheet access to the inner magnetosphere, *J. Geophys. Res.*, *106*, 5845–5858.

Fok, M.-C., R. B. Horne, N. P. Meredith, and S. A. Glauert (2008), Radiation belt environment model: Application to space weather nowcasting, *J. Geophys. Res.*, *113*, A03S08, doi:10.1029/2007JA012558.

Fälthammar, C.-G. (1965), Effects of time-dependent electric fields on geomagnetically trapped radiation, *J. Geophys. Res.*, *70*, 2503.

Ganushkina, N. Yu. (2011), IMPTAM: Including self-consistent magnetic field in ring current modeling, *Oral presentation at 2011 Joint CEDAR-GEM workshop*, 26 June–1 July, Santa Fe, NM, USA.

Ganushkina, N. Yu., S. Dubyagin, M. Kubyshkina, M. Liemohn, and A. Runov (2012a), Inner magnetosphere currents during CIR/HSS storm on July 21–23, 2009, *J. Geophys. Res.*, in press, doi:10.1029/2011JA017393.

Ganushkina, N., M. Liemohn, M. Kubyshkina, R. Ilie, and H. Singer (2010), Distortions of the magnetic field by storm-time current systems in earth's magnetosphere, *Ann. Geophys.*, *28*, 123–140, doi:10.5194/angeo-28-123-2010.

Ganushkina N. Yu., M. W. Liemohn, and T. I. Pulkkinen (2012b), Storm-time ring current: Model-dependent results, *Ann. Geophys.*, *30*, 177–202, doi:10.5194/angeo-30-177-2012.

Ganushkina, N. Y., T. I. Pulkkinen, V. F. Bashkirov, D. N. Baker, and X. Li (2001), Formation of intense nose structures, *Geophys. Res. Lett.*, *28*(3), 491–494.

Ganushkina, N. Yu., T. I. Pulkkinen, and T. Fritz (2005), Role of substorm-associated impulsive electric fields in the ring current development during storms, *Ann. Geophys.*, *23*, 579–591, doi:10.5194/angeo-23-579-2005.

Ganushkina, N., T. I. Pulkkinen, M. Liemohn, and A. Milillo (2006), Evolution of the proton ring current energy distribution during April 21–25, 2001 storm, *J. Geophys. Res.*, *111*, A11S08, doi:10.1029/2006JA011609.

Glocer, A., M.-C. Fok, T. Nagai, G. Toth, T. Guild, and J. Blake (2011), Rapid rebuilding of the outer radiation belt, *J. Geophys. Res.*, *116*, A09213, doi:10.1029/2011JA016516.

Horne, R. B., N. P. Meredith, S. A. Glauert, A. Varotsou, R. M. Thorne, Y. Y. Shprits, and R. R. Anderson (2006), Mechanisms for the acceleration of radiation belt electrons, in *Recurrent Magnetic Storms: Corotating Solar Wind Streams*, Geophys. Monogr. Ser., vol. *167*, edited by B. T. Tsurutani, R. L. McPherron, W. D. Gonzalez, G. Lu, J. H. A. Sobral, and N. Gopalswamy, pp. 151–173, AGU, Washington, D.C.

Horne, R. B., and R. M. Thorne (2003), Relativistic electron acceleration and precipitation during resonant interactions with whistler-mode chorus, *Geophys. Res. Lett.*, *30*(10), 1527, doi:10.1029/2003GL016973.

Huang, C. Y., and L. A. Frank, (1986) A statistical study of the central plasma sheet: Implications for substorm models, *Geophys. Res. Lett.*, *13*, 652–655.

Ingraham, J. C., T. E. Cayton, R. D. Belian, R. A. Christensen, R. H. W. Friedel, M. M. Meier, G. D. Reeves, and M. Tuszewski (2001), Substorm injection of relativistic electrons to geosynchronous orbit during the great magnetic storm of March 24, 1991, *J. Geophys. Res.*, *106*, 25,759–25,776.

Jordanova, V. K., L. M. Kistler, J. U. Kozyra, G. V. Khazanov, and A. F. Nagy, (1996) Collisional losses of ring current ions, *J. Geophys. Res.*, *101*(A1), doi:10.1029/95JA02000.

Jordanova, V. K., L. M. Kistler, M. F. Thomsen, and C. G. Mouikis (2003), Effects of plasma sheet variability on the fast initial ring current decay, *Geophys. Res. Lett.*, *30*(6), 1311, doi:10.1029/2002GL016576.

Kaufmann, R. L., W. R. Paterson, and L. A. Frank (2005), Relationships between the ion flow speed, magnetic flux transport rate, and other plasma sheet parameters, *J. Geophys. Res.*, *110*, A09216, doi:10.1029/2005JA011068.

Kerns, K. J., D. A. Hardy, and M. S. Gussenhoven (1994), Modeling of convection boundaries seen by CRRES in 120-eV to 28-keV particles, *J. Geophys. Res.*, *99*(A2), 2403–2414, doi:10.1029/93JA02767.

Kim, H. J., and A. A. Chan (1997), Fully adiabatic changes in storm time relativistic electron fluxes, *J. Geophys. Res.*, *102*, 22,107-22,116, doi:10.1029/97JA01814.

Kurita, S., et al. (2011), Transport and loss of the inner plasma sheet electrons: THEMIS observations, *J. Geophys. Res.*, *116*, A03201, doi:10.1029/2010JA015975.

Li, X., D. N. Baker, M. Temerin, G. D. Reeves, and R. D. Belian (1998), Simulation of dispersionless injections and drift echoes of energetic electrons associated with substorms, *Geophys. Res. Lett.*, *25*, 3763–3766.

Li, X., T. E. Sarris, D. N. Baker, W. K. Peterson, and H. J. Singer (2003), Simulation of energetic particle injections associated with a substorm on August 27, 2001, *Geophys. Res. Lett.*, *30*, 1004, doi:10.1029/2002GL015967.

Liu, W. L., X. Li, T. Sarris, C. Cully, R. Ergun, V. Angelopoulos, D. Larson, A. Keiling, K. H. Glassmeier, and H. U. Auster (2009), Observation and modeling of the injection observed by THEMIS and LANL satellites during the 23 March 2007 substorm event, *J. Geophys. Res.*, *114*, A00C18, doi:10.1029/2008JA013498.

Lyons, L. R., D.-Y. Lee, R. M. Thorne, R. B. Horne, and A. J. Smith (2005), Solar wind-magnetosphere coupling leading to relativistic electron energization during high-speed streams, *J. Geophys. Res.*, *110*, A11202, doi:10.1029/2005JA011254.

Lyons, L. R., Y. Nishimura, X. Xing, A. Runov, V. Angelopoulos, E. Donovan, and T. Kikuchi (2012), Coupling of dipolarization front flow bursts to substorm expansion phase phenomena within the magnetosphere and ionosphere, *J. Geophys. Res.*, *117*, A02212, doi:10.1029/2011JA017265.

Maynard, N. C., W. J. Burke, E. M. Basinska, G. M. Erickson, W. J. Hughes, H. J. Singer, A. G. Yahnin, D. A. Hardy, and F. S. Mozer (1996), Dynamics of the inner magnetosphere near times of substorm onsets,*J. Geophys. Res.*, *101*(A4), 7705–7736, doi:10.1029/95JA03856.

Mauk, B. H., and C. I. Meng (1983), Dynamical injections as the source of near geostationary quiet time particle spatial boundaries, *J. Geophys. Res.*, *88*(A12), 10,011–10,024, doi:10.1029/JA088iA12p10011.

Meredith, N. P., R. B. Horne, and R. R. Anderson (2001), Substorm dependence of chorus amplitudes: Implications for the acceleration of electrons to relativistic energies, *J. Geophys. Res.*, *106*, 13,165–13,178.

Mithaiwala, M. J., and W. Horton (2005), Substorm injections produce sufficient electron energization to account for MeV flux enhancements following some storms, *J. Geophys. Res.*, *110*, A07224, doi:10.1029/2004JA010511.

Miyoshi, Y. S., V. K. Jordanova, A. Morioka, M. F. Thomsen, G. D. Reeves, D. S. Evans, and J. C. Green (2006), Observations and modeling of energetic electron dynamics during the October 2001 storm, *J. Geophys. Res.*, *111*, A11S02, doi:10.1029/2005JA011351.

Nakamura, R., et al. (2002), Motion of the dipolarization front during a flow burst event observed by Cluster, *Geophys. Res. Lett.*, *29*(20), 1942, doi:10.1029/2002GL015763.

Ohtani, S. (1998), Earthward expansion of tail current disruption: Dual-satellite study, *J. Geophys. Res.*, *103*(A4), 6815–6825, doi:10.1029/98JA00013.

Parker, E. N., and H. A. Stewart (1967), Nonlinear inflation of a magnetic dipole, *J. Geophys. Res.*, *72*, 5287.

Pierrard, V., G. V. Khazanov, J. Cabrera, and J. Lemaire (2008), Influence of the convection electric field models on predicted plasmapause positions during magnetic storms, *J. Geophys. Res.*, *113*, A08212, doi:10.1029/2007JA012612.

Pulkkinen, T. I., Ganushkina, N. Yu., Donovan, E., Li, X., Reeves, G. D., Russell, C. T., Singer, H. J., and J. A. Slavin (2005) Storm-substorm coupling during 16 hours of Dst steadily at 150 nT, in *The Inner Magnetosphere: Physics and Modeling*, Geophysical Monograph, vol. *155*, edited by T. I. Pulkkinen, N. A. Tsyganenko, and R. H. W. Friedel, pp. 155–161, AGU, Washington, D.C.

Reeves, G. D., M. G. Henderson, P. S. McLachlan, R. D. Belian, R. H. W. Friedel, and A. Korth (1996) Radial propagation of substorm injections, *Proceedings of the 3rd International Conference on Substorms*, Versailles, France, 12–17 May, pp. 579–584.

Roederer, J. G. (1970), *Dynamics of Geomagnetically Trapped Radiation*, 36 pp., Springer-Verlag, New York.

Rowland, D. E., and J. R. Wygant (1998), Dependence of the large-scale, inner magnetospheric electric field on geomagnetic activity, *J. Geophys. Res.*, *103*(A7), 14,959–14,964, doi:10.1029/97JA03524.

Runov, A., V. Angelopoulos, and X.-Z. Zhou (2012), Multipoint observations of dipolarization front formation by magnetotail reconnection, *J. Geophys. Res.*, *117*, A05230, doi:10.1029/2011JA017361.

Runov, A., V. Angelopoulos, X.-Z. Zhou, X.-J. Zhang, S. Li, F. Plaschke, and J. Bonnell (2011), A THEMIS multicase study of dipolarization fronts in the magnetotail plasma sheet, *J. Geophys. Res.*, *116*, A05216, doi:10.1029/2010JA016316.

Sarris, T. E., and X. Li (2005), Evolution of the dispersionless injection boundary associated with substorms, *Ann. Geophys.*, *23*, 877–884, doi:10.5194/angeo-23-877-2005.

Sarris, T. E., X. Li, N. Tsaggas, and N. Paschalidis (2002), Modeling energetic particle injections in dynamic pulse fields with varying propagation speeds, *J. Geophys. Res.*, *107*, 1033, doi:10.1029/2001JA900166.

Sergeev, V., V. Angelopoulos, S. Apatenkov, J. Bonnell, R. Ergun, J. McFadden, D. Larson, R. Nakamura, and A. Runov (2009), Structure of injection front in the flow braking region, *Geophys. Res. Lett.*, *36*, L21105, doi:10.1029/2009GL040658.

Schulz, M., and L. Lanzerotti (1974), *Particle Diffusion in the Radiation Belts*, Springer, New York.

Scudder, J., et al. (1995), Hydra: A 3-dimensional electron and ion hot plasma instrument for the Polar spacecraft of the GGS mission, *Space Sci. Rev.*, *71*, 459–495.

Sergeev, V. A., Shukhtina, M. A., Rasinkangas, R., Korth, A., Reeves, G. D., Singer, H. J., Thomsen, M. F., and Vagina, L. I. (1998), Event study of deep energetic particle injections during substorm, *J. Geophys. Res.*, *103*(A5), 9217–9234, doi:10.1029/97JA03686, 1998.

Slavin, J. A., et al. (2002), Simultaneous observations of earthward flow bursts and plasmoid ejection during magnetospheric substorms, *J. Geophys. Res.*, *107*(A7), 1106, doi:10.1029/2000JA003501.

Shepherd, G. G., R. Bostrom, H. Derblom, C.-G. Falthammar, R. Gendrin, K. Kaila, A. Korth, A. Pedersen, R. Pellinen, and G. Wrenn (1980), Plasma and field signatures of poleward propagating auroral precipitation observed at the foot of the Geos 2 field line, *J. Geophys. Res.*, *85*(A9), 4587–4601, doi:10.1029/JA085iA09p04587.

Shprits, Y. Y., N. P. Meredith, and R. M. Thorne (2007), Parameterization of radiation belt electron loss timescales due to interactions with chorus waves, *Geophys. Res. Lett.*, *34*, L11110, doi:10.1029/2006GL029050.

Shprits, Y. Y., D. Subbotin, and B. Ni (2009), Evolution of electron fluxes in the outer radiation belt computed with the VERB code, *J. Geophys. Res.*, *114*, A11209, doi:10.1029/2008JA013784.

Shprits Y. Y., and R. M. Thorne (2004), Time dependent radial diffusion modeling of relativistic electrons with realistic loss rates, *Geophys. Res. Lett.*, *31*, L08805, doi:10.1029/2004GL019591.

Stern, D. (1975), The motion of a proton in the equatorial magnetosphere, *J. Geophys. Res.*, *80*(4), 595–599.

Taylor, M. G. G. T., R. H. W. Friedel, G. D. Reeves, M. W. Dunlop, T. A. Fritz, P. W. Daly, and A. Balogh (2004), Multisatellite measurements of electron phase space density gradients in the Earth's inner and outer magnetosphere, *J. Geophys. Res.*, *109*, A05220, doi:10.1029/2003JA010294.

Tóth, G., et al. (2005), Space weather modeling framework: A new tool for the space science community, *J. Geophys. Res.*, *110*, A12226, doi:10.1029/2005JA011126.

Tsyganenko, N. A. (1995), Modeling the Earth's magnetospheric magnetic field confined within a realistic magnetopause, *J. Geophys. Res.*, *100*, 5599–5612.

Tsyganenko, N. A., and T. Mukai (2003), Tail plasma sheet models derived from Geotail particle data, *J. Geophys. Res.*, *108*(A3), 1136, doi:10.1029/2002JA009707.

Tsyganenko, N. A., H. J. Singer, and J. C. Kasper (2003), Storm-time distortion of the inner magnetosphere: How severe can it get?, *J. Geophys. Res.*, *108*(A5), 1209, doi:10.1029/2002JA009808.

Tsyganenko, N. A., and M. I. Sitnov (2005), Modeling the dynamics of the inner magnetosphere during strong geomagnetic storms, *J. Geophys. Res.*, *110*, A03208, doi:10.1029/2004JA010798.

Tu, J.-N., K. Tsuruda, H. Hayakawa, A. Matsuoka, T. Mukai, I. Nagano, and S. Yagitani (2000), Statistical nature of impulsive electric fields associated with fast ion flow in the near-Earth plasma sheet, *J. Geophys. Res.*, *105*(A8), 18,901–18,907, doi:10.1029/1999JA000428.

Varotsou, A., D. Boscher, S. Bourdarie, R. B. Horne, S. A. Glauert, and N. P. Meredith (2005), Simulation of the outer radiation belt electrons near geosynchronous orbit including both radial diffusion and resonant interaction with whistler-mode chorus waves, *Geophys. Res. Lett.*, *32*, L19106, doi:10.1029/2005GL023282.

Volland, H. (1973), A semi-empirical model of large-scale magnetospheric electric fields, *J. Geophys. Res.*, *78*(1), 171–180.

Wang, C.-P., M. Gkioulidou, L. R. Lyons, and V. Angelopoulos (2012), Spatial distributions of the ion to electron temperature ratio in the magnetosheath and plasma sheet, *J. Geophys. Res.*, *117*, A08215, doi:10.1029/2012JA017658.

Wang, C.-P., M. Gkioulidou, L. R. Lyons, R. A. Wolf, V. Angelopoulos, T. Nagai, J. M. Weygand, and A. T. Y. Lui (2011), Spatial distributions of ions and electrons from the plasma sheet to the inner magnetosphere: Comparisons between THEMIS-Geotail statistical results and the Rice convection model, *J. Geophys. Res.*, *116*, A11216, doi:10.1029/2011JA016809.

Wygant, J., D. Rowland, H. J. Singer, M. Temerin, F. Mozer, and M. K. Hudson (1998), Experimental evidence on the role of the large spatial scale electric field in creating the ring current, *J. Geophys. Res.*, *103*(A12), 29,527–29,544, doi:10.1029/98JA01436.

Zaharia, S., C. Z. Cheng, and J. R. Johnson (2000), Particle transport and energization associated with substorms, *J. Geophys. Res.*, *105*(A8), 18,741–18,752, doi:10.1029/1999JA000407.